Politecnico di Milano
School of Industrial and Information Engineering
Master of Science in Aeronautical Engineering

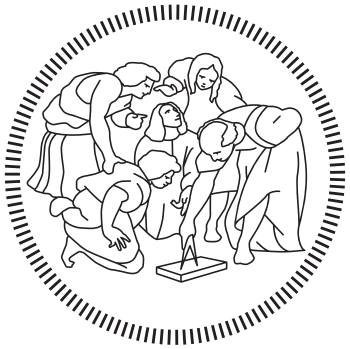

A statistical analysis of position estimation errors in visual odometry

Advisor: Prof. Marco LOVERA
Eng. Gabriele ROGGI

Thesis by:
Federico CHIARLO Matr. 919926

Academic Year 2020–2021

A Flavio ed Emma.

Acknowledgments

Vorrei in primis porgere i miei ringraziamenti al Professor Marco Lovera e all'Ing. Gabriele Roggi, per avermi seguito ed aiutato in questi mesi con grande disponibilità e gentilezza. Da questo percorso ho imparato molto, non solo a livello tecnico.

Mi è poi impossibile descrivere a parole il senso di gratitudine verso i miei genitori e verso Mauro, Cinzia, la Nonna Marisa, il Nonno, e la Nonna Elsa, ma sono sicuro che loro lo sanno già. Hanno sacrificato molto per concedermi questa opportunità, e questo traguardo è anche il loro. Un enorme grazie va poi a zio Giulio, zia Marina e zia Giuliana, e alla famiglia savonese per avermi aiutato e spronato: Angela, Davide, Andre, Matte e Carmela.

Per quanto riguarda gli amici, i ringraziamenti richiederebbero una tesi a parte. Evitando un asettico elenco (che poi se dimentico qualcuno è la fine), voglio ringraziare tutte e tutti, dai milanesi (coinquilini e non) ai genovesi, fino - addirittura - a quelli che vanno a spiaggia. Questo non è un ringraziamento pro forma: sono immensamente grato di avervi conosciuto, non solo per le avventure assurde e per la compagnia durante questo viaggio lombardo, ma perché standovi vicino ho imparato, tra le mille altre cose, che i miei limiti sono quasi sempre autoimposti, e che realizzare ciò comporta una costante e bellissima liberazione.

Un grazie a parte ad Andre, compagno di gioie e fatiche politecniche, per il suo sincero e costante supporto.

Abstract

Over the last decade, visual odometry has become a key feature of unmanned ground and aerial vehicles. The decrease in costs of cameras and computational power have made this technology a valuable alternative to other kinds of navigation systems.

In many applications, visual odometry is coupled with systems such as GPS and INS to improve the overall performance. However, while the errors affecting GPS and INS have been widely studied and described in literature, no attempts in characterizing the dynamics of the noise of visual odometry systems have been made.

The aim of this thesis is to investigate these noise dynamics. Sixteen different experiments were performed with a drone estimating its position by means of a stereoscopic camera. The noise affecting the visual odometry process has been analyzed with a statistical, time-domain-based method called Allan Variance, and the results of the experiments have been compared to understand how different choices of some flight and environmental parameters can change the characteristics of the noise dynamics.

Lastly, a Kalman predictor has been constructed to compare the noise dynamics obtained from the analysis with the dynamics of the real noise measured.

Sommario

Nel corso dell'ultimo decennio, l'odometria visiva è diventata una caratteristica sempre più importante per i veicoli autonomi, sia terrestri che aerei. Il ridursi dei costi di potenza computazionale e delle videocamere hanno reso questa tecnologia una conveniente alternativa ad altre tipologie di sistemi di navigazione.

In molte applicazioni, l'odometria visiva è accoppiata a sistemi come il GPS e l'INS per aumentare la performance totale. Tuttavia, mentre gli errori che affliggono il GPS e l'INS sono stati ampiamente studiati e descritti in letteratura, nessuna caratterizzazione della dinamica dei rumori agenti sui sistemi di odometria visiva è mai stata oggetto di studio.

L'obiettivo di questa tesi è investigare tale dinamica. Sono stati compiuti sedici diversi esperimenti, in cui un drone ha stimato la propria posizione per mezzo di una videocamera stereoscopica. Il rumore agente sul sistema di odometria visiva è stato analizzato tramite un metodo statistico chiamato Varianza di Allan, e i risultati degli esperimenti sono stati confrontati tra loro per osservare come differenti scelte di alcuni parametri - di volo e ambientali - possono modificare le caratteristiche del rumore.

Infine, è stato costruito un predittore di Kalman per comparare la dinamica del rumore ottenuta dall'analisi con quella del rumore misurato.

Contents

List of Figures

List of Tables

Introduction

Visual odometry is the technique of estimating the motion of a body by comparing pictures taken by one or more cameras mounted on the body itself.

These techniques, starting from '80s, were studied and implemented by NASA for the 2004 Mars Mission. In recent years, the strong drop of the costs of cameras and CPU have made this technology relatively inexpensive when compared to other kinds of self-contained motion estimation systems, such as Inertial Navigation Systems (INS) and LIDAR. Nowadays, industries of both unmanned ground vehicles (UGVs) and unmanned aerial vehicles (UAVs) make large use of visual odometry, coupled with other systems such as GPS and INS, to greatly improve the precision of motion estimation. Visual odometry techniques present also the advantage of being a convenient method to perform SLAM (Simultaneous Localization And Mapping).

Despite the effort to improve the performance of visual odometry systems, both in terms of computational speed and precision, no direct attempt has been made to characterize and evaluate the dynamics of the noise affecting said systems. The availability of a description of these dynamics, which for other systems - such as INS and GPS - are already well known, would be a great benefit in a sensor-fusion-oriented framework.

In this thesis, by means of a statistical, time-domain noise analysis technique known as Allan Variance, a method is presented to characterize the noise affecting the visual odometry system both in terms of Power Spectral Density (PSD) and state space representation.

Thesis structure

This thesis is organized in two main Chapters:

- In Chapter 1, the Allan Variance (AVAR) is introduced. Several types of noises are then described in terms of their PSD and of their representation in the AVAR-based analysis.

  An example of AVAR analysis of a signal is then presented, showing how each fundamental noise can be isolated and evaluated, and how the PSD of

the total noise and its dynamics' time-continuous state space representation can be approximated.

- In Chapter 2, the noise characterization of a drone's visual odometry system is presented.

  Sixteen different experiments have been performed, each one with similar flight trajectory but different choices of four parameters: trajectory height, speed, ambient light and yaw following mode inactive or active.

  In each experiment, the noise affecting the position estimation has been measured by comparing the motion evaluated by the visual odometry system (a Stereolab ZED camera) with the ground truth from a Motion Capture system.

  The results of each experiment are presented, and they are compared to each other in order to investigate how the above-described parameters influence the dynamics of the noise.

  A Kalman predictor is then constructed in order to compare the AVAR-based model of the noise to the real noise measured during the experiments.

Chapter 1

Allan variance and noise characterization

1.1 The Allan variance

In this chapter, the methodology of the Allan variance-based noise analysis is presented.

After the definition of Allan variance and its variants, a list of fundamental noises is introduced. These noises will be used to approximate the real noise acting on the system: the Allan variance indicates which noises are needed and how strong their intensities have to be in order to obtain a valid approximation.

The chapter ends with an example of noise analysis.

1.1.1 Allan variance definition

The Allan Variance (AVAR) is a mathematical tool created by David Allan in 1966 to study the error in frequency of atomic clocks. It has been later applied to characterize and quantify noises affecting the rate gyros in Inertial Measurement Units (IMU).

Some conceptual aspects behind the AVAR have a slightly different interpretation depending on the nature of the considered system. Indeed, the original definition from David Allan is given starting from a frequency framework - then translated to time domain - because the studied systems were clocks. In this thesis, AVAR's definition and the subsequent interpretation are presented in a time-domain framework, being the time history of the error between a variable and its estimate the subject of study. This approach is typical of AVAR-based analysis of IMU rate gyros [1]. If one desires to know more about David Allan original work, see [2].

To understand the meaning of the AVAR, it should be first considered how it is computed. The starting point is an array of n values y_i, $i = 1, 2, 3...$ representing the time history of the stochastic error of interest. All the deterministic

sources of noise should be filtered out before beginning the analysis. The AVAR calculation requires an array with constant sampling interval τ_0 - even though small oscillations due to jitter may not compromise the results - and with no dead time ("holes" in the array). If some sparse points are missing they can be reconstructed by interpolation, but if there is a massive gap in the array the results may be incorrect.

The array is split into M clusters - of subsequent points - of equal length τ. This length can be any integer number comprised between $\tau = 1$ and $\tau = floor(n/2)$, where the floor function is considered in case the number of samples in the dataset is odd, so that a cluster cannot have length greater than $\tau = n/2$. The generic τ is often described as an integer multiple of the sampling interval τ_0, such that $\tau = m\tau_0$. The value m is called Averaging Factor. If, for a certain m, τ is not a divisor of n, it can be skipped or the computation can be performed neglecting the last points of the array which are not enough to form the last cluster.

For each cluster, a new value is then obtained by computing the average of all the points contained in that single cluster. This process, visualized in Figure 1.1, leads to a new array of $M(\tau)$ averaged values. The AVAR, for the selected τ, is the "classic" variance of these M averaged values.

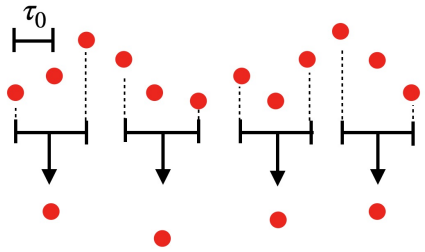

Figure 1.1: Visualization of the AVAR computation for $m = 2$, so that $\tau = 2\tau_0$. The initial array is split into clusters of 3 points each. The average of each cluster has been computed, obtaining a new set of values. The AVAR for $\tau = 2\tau_0$ is the variance of this new set.

Naming $\bar{y}_i$ as the average of the i-th cluster, which depends on τ, the above-described process leads to the following definition of the AVAR $\sigma^2(\tau)$:

$$\sigma^2(\tau) = \frac{1}{2(M-1)} \sum_{i=1}^{M-1} \left[\bar{y}_{i+1} - \bar{y}_i\right]^2 \tag{1.1}$$

where $\bar{y}_i$ is the average of the i-th cluster, which depends on τ.

To summarize, the AVAR describes how the variance computed after the averaging process changes in relation to the length of the clusters.

For example, by checking for which value of m the AVAR reaches its minimum, one can know how many subsequent points have to be averaged in order to obtain a

new measurement array, of length n/m, characterized by the lowest possible noise. A possible downside of this choice may be the loss of high frequency dynamics. This aspect of the AVAR is useful, for instance, in sensors comparison.

The results are usually plotted in a log-log scale plot. The x-axis is not directly expressed in terms of τ, but in terms of the product between τ and the inverse of the sample frequency, in Hertz, of the initial array. Even though by doing so the relation with the cluster length is not immediately readable on the plot, this is convenient: indeed, as will be shortly explained, the AVAR can be divided into different regions, each giving information about a specific type of noise. Given a point on the AVAR, the shape of the curve in the neighbourhood of that point is related to the type of noise, while the value on the time axis, in seconds, is the time scale at which that noise type is the dominant one.

This also means that the same data set will have different AVAR plot if the sample frequency changes.

An example of AVAR plot is shown in Figure 1.2.

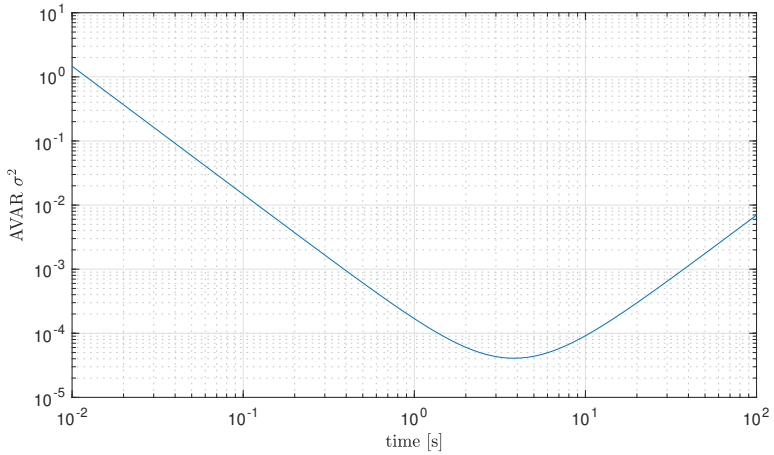

Figure 1.2: Example of AVAR plot.

1.1.2 Allan deviation and overlapped AVAR

The AVAR is seldom used to perform the noise characterization of a signal. What it usually examined is the log-log plot of its square root, the Allan Deviation (ADEV). The reasons behind this choice will be clear in the next pages.

Furthermore, the previously introduced AVAR estimator is quite inaccurate, in particular for large values of τ. As reported in page 10 of [3], when τ exceeds 10% of the total measurement time the uncertainty on the ADEV becomes very high. This is why to compute the AVAR a better estimator called Overlapped AVAR Estimator is generally applied. It differs in the fact that the clusters can overlap, while in the AVAR calculation if a cluster ends in point i then the next

one begins in point $i+1$. If the overlapping is maximum (which is, when a cluster begins in point i then the next one begins in point $i+1$, as shown in Figure 1.3), the Overlapped AVAR is called Maximum Overlapped AVAR. The estimator for the Maximum Overlapped AVAR is (from [4]):

$$\sigma^2(\tau) = \frac{1}{2(n-2m)m^2\tau_0^2} \sum_{i=1}^{n-2m} \left[x_{i+2m} - 2x_{i+m} + x_i \right]^2 \tag{1.2}$$

where x are the values of the initial noise array, n is the total number of said values and m is the averaging factor.

The Overlapped AVAR (both "not-maximum" and "maximum") is the recommended estimator for the Allan Variance by the IEEE standard. Its confidence interval can be computed making use of the chi-square distribution as shown in Chapter V and VI of [5]. More information about the different AVAR variants (Modified AVAR, Dynamic AVAR) and other kinds of variances can be found in [3].

In MATLAB, the AVAR is computed with the function "allanvar".

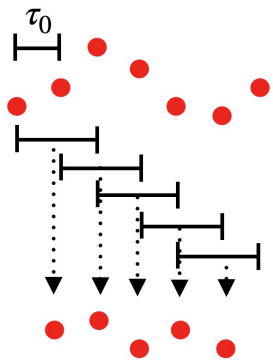

Figure 1.3: Visualization of the Maximum Overlapped AVAR computation for $m = 2$. The AVAR estimate for such value of m is the variance of the new set of points.

1.2 ADEV-based noise characterization

1.2.1 Analysis outline

The AVAR has become a standard in IMU noise analysis thanks to its capability to provide easily and quickly an approximation of the dynamics of the noise in terms both of Power Spectral Density (PSD) and, under some restrictions, of state space representation.

This noise characterization method is based on the relation between the AVAR representation of a noise and its PSD. These two quantities are linked by the integral transformation:

$$\sigma^2(\tau) = 4 \int_0^\infty S(f) \frac{\sin^4(\pi f \tau)}{(\pi f \tau)^2} \, df \tag{1.3}$$

where $S(f)$ is the PSD of the noise, function of the frequency f. More specifics about how this equation is obtained can be found in Section 4.2 of [6]. Unfortunately, this transformation has no inverse formula.

Once the AVAR-PSD transformation has been introduced, the analysis can be summarized in the following steps:

- Starting from the time history of the noise, remove the sources of deterministic errors.
- Compute the ADEV of the noise by first calculating the AVAR and then its square root, and plot it in log-log scale.
- Once the ADEV plot is available, one has to construct a "dummy ADEV" which has to resemble the "original ADEV" as close as possible.

  To create the dummy ADEV there are several fundamental noises, each one having its own PSD which, through the transformation (1.3), is associated with a particular ADEV plot. The dummy curve is the sum of all these different ADEV contributions. By tuning the intensities of the PSDs of the noises - the noise coefficients - one has to shape the dummy ADEV to make it overlap as close as possible to the original one.

  Once the right shape has been drawn, the resulting coefficients are the ones that approximate the characteristics of the original noise. The list of fundamental noises is reported in Section 1.2.2. For each noise a quick approach to find a first guess for its coefficient is available. Most of the time the coefficients have to be further tuned considering the other noises' contributions.

  An example is provided after the list, in Section 1.2.3.
- Once the coefficients are known, the estimated PSD of the original noise can be computed just by summing the PSDs of all the considered fundamental noises.
- The list of noises contains also their contribution to the final state space representation. The procedure to "assemble" it is reported in Section 1.2.4.

  Due to the nature of their PSDs, some noises cannot provide a direct contribution. If the state space representation is required and these noise are needed to reconstruct the dummy ADEV, there are two possible options: one can avoid using them and accept lower accuracy in the results, or one

can construct a state space representation with approximation techniques starting from the total estimated PSD.

The generic system representing the noise dynamics is:

$$\begin{cases} \dot{x}(t) = Ax(t) + Bu(t) & \text{State equation} \\ z(t) = Cx(t) + Dv(t) & \text{Output equation} \end{cases} \tag{1.4}$$

where:

- $x(t)$ is the state vector representing the values of the different fundamental noises;
- $u(t)$ is a vector whose components are independent white Gaussian noises called "driving" noises. Indeed, as will be shortly explained, most of the fundamental noises that have a state space representation are expressed in terms of processes taking as input a white noise.
- $v(t)$ is a scalar white Gaussian noise representing a specific noise yet to be introduced.
- The output $z(t)$ is the total estimated noise.

The dimensions of these vectors, as well as those of the matrix A, B and C, depend on the fundamental noises considered. The matrix D is always $D = 1$.

1.2.2 Fundamental noises

What follows is a list of the main noise types involved in the AVAR analysis. Their intensities, in terms of PSD coefficients, will be obtained by the ADEV plots. These plots will have the x-axis expressed in terms of τ because, to present them, a sampling frequency equal to 1 Hz has been chosen and therefore the time-axis and the τ-axis are equivalent (see end of Section 1.1.1).

Most of the noises have a PSD described by the power law $S(f) = \beta f^{-\alpha}$ where f is the frequency, α is the power law coefficient and β is a fixed value related to the noise coefficient.

Noises with ADEV plot characterized by a straight line with slope -1:

This first fundamental ADEV plot is not applied in this thesis, but it is reported for completeness. It requires a conceptual distinction depending on the nature of the system, because it can be associated with different fundamental noises.

- When the system in study is a rate gyro or an accelerometer, a noise with ADEV slope equal to -1 is often called quantization noise, because in IMUs it is generated by the process of encoding an analog signal. For a rate gyro the quantization noise PSD, as reported in section II.C.1 of [1], is approximable as:

$$S_Q(f) \approx (2\pi f)^2 T_s Q_z^2 \qquad f < \frac{1}{2T_s} \tag{1.5}$$

where Q_z is the quantization noise coefficient and T_s the sampling interval. Substituting this PSD in equation (1.3), the ADEV becomes:

$$\sigma(\tau) = \sqrt{3}\frac{Q_z}{\tau} \tag{1.6}$$

Therefore, as shown in Figure 1.4, a pure quantization noise has ADEV plot represented by a line with slope -1. The intensity of the PSD Q_z can be easily read by looking at the ADEV value for $\tau = \sqrt{3}$. If other noises are present and the region having slope -1 lies in a range of τ far from $\sqrt{3}$, to obtain the coefficient Q_z one can extend the line until it reaches said value of τ and read the corresponding ADEV intensity.

If, as it is most of the times, the quantization noise is mixed with other noises, there are some issues that must be taken into account.

First of all, if the other noises are stronger than the quantization one, it might not appear in the ADEV plot. Indeed, even if it grows as τ becomes smaller, the range of τ in which the AVAR is available - which depends on the data and the sampling frequency - may not be large enough to let the quantization noise reach a sufficiently high value to appear in the plot.

A second issue is that, even if the ADEV presents a region resembling a straight line with slope -1, it may be associated to other kinds of noises. More information will be given discussing the next noise type.

- If the system is not an IMU, one can follow the original approach by David Allan, considering ideal noises defined by their own PSDs. Two different fundamental noises can produce an ADEV with slope -1: the white phase noise and the flicker phase noise.

The white phase noise presents a Power-Law-type PSD with $\alpha = -2$ (that is, the PSD is proportional to f^2) while the flicker phase noise has PSD with power law coefficient $\alpha = -1$. If the distinction between these two noises is required, a convenient solution is the modified Allan variance (Mod σ^2). It is a variation of the AVAR which assumes slightly different slopes when representing these two noises, with the downside that it requires more

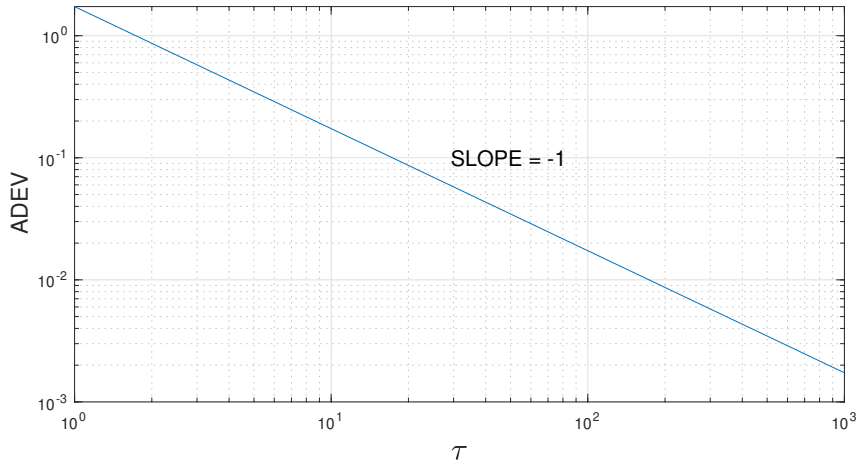

Figure 1.4: Example of an ideal ADEV plot for pure quantization noise
Example of an ideal ADEV plot for pure quantization noise, with $Q_z = 1$.

computation than the AVAR. More information about this kind of noises and the modified AVAR can be found in [3]. [7] and [4]. An algorithm to identify these noises and calculate their PSD intensities is shown in Chapter 5.5 of [4].

Angular random walk (ARW) - Velocity random walk - White frequency noise

The second type of noise is the white frequency noise, with constant PSD $Q_N = N^2$. In rate gyro analysis framework it often takes the name Angular Random Walk (ARW). When the system is an accelerometer, it is usually called Velocity Random Walk. To avoid confusion, from now on it will be just called ARW.

Substituting its PSD in equation (1.3), the AVAR becomes $\sigma^2(\tau) = N^2/\tau$ and therefore the ADEV of the ARW is :

$$\sigma(\tau) = \frac{N}{\sqrt{\tau}} \tag{1.7}$$

The ADEV plot in log-log scale is a straight line with slope $-1/2$ and the PSD coefficient N can be easily obtained by looking at the ADEV value for $\tau = 1$. If other noises are present and the region with this slope is far from $\tau = 1$, one can just prolong the straight line until said point is met. An example of ARW ADEV plot is shown in Figure 1.5.

For a pure ARW noise, in the system (1.4) there is no state equation because the ARW contribution to the state space representation is a single white Gaussian noise ω_N, with PSD $Q_N = N^2$, as forcing term in the output equation (direct

transmission term). Indeed, this noise type has no dynamics and the state space representation is reduced to:

$$z(t) = z_N(t) = \omega_N(t) \tag{1.8}$$

where $z_N(t)$ is the contribution of the ARW to the total noise $z(t)$.

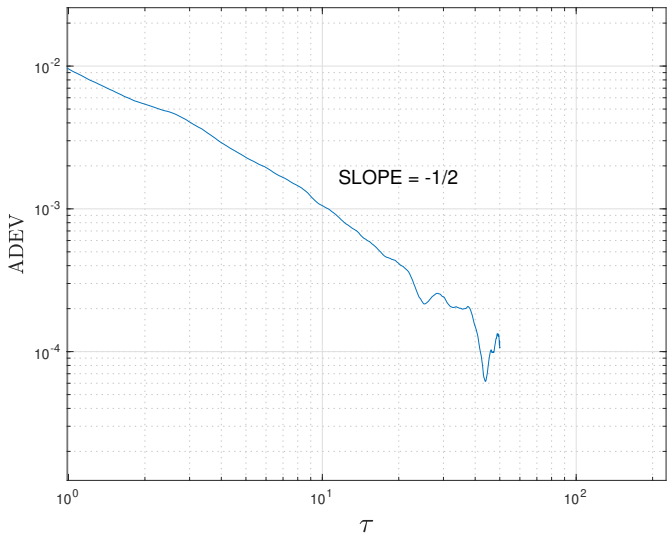

Figure 1.5: Example of ADEV plot of a randomly generated white noise. Some small oscillations for low τ are due to the random process, while for high τ they are caused by uncertainties in the ADEV computation. The noise coefficient is $N = 0.01$ and indeed the curve, approximated by a line with slope -1/2, for $\tau = 1$ is $\sigma(1) \simeq 0.01$.

A critical aspect of the ARW is noteworthy: as will be better explained in Section 1.2.2, not all the regions resembling a line with slope -1/2 can be associated with this noise.

Furthermore, as for the quantization noise, the ARW may be present in the signal but may not show up in the plot if other noises are more intense, or if the range on the time axis where the ADEV is available does not cover the values of t where the ARW is the dominant noise.

Sometimes the initial part of the ADEV plot may be decreasing with a slope less intense in absolute value than -1/2, and then increasing for the presence of other noises. In this case one can approximate this shape by introducing a low ARW noise and construct the Dummy ADEV by summing it with other more intense noises, in order to get as near as possible to the original ADEV. An example is given at the end of section 1.2.3.

Lastly, considering Figure 1.5 as example, one has to be aware that for large τ there might by some oscillations where small regions similar to straight lines with

slope -1/2 may appear, but this part of the plot (in this specific case, for $\tau > 11$) has to be considered unreliable due to the large uncertainty. This is valid for any noise, not just for the ARW.

Rate random walk (RRW) - Acceleration random walk - Random walk frequency noise

The random walk frequency noise is defined by a power law PSD with $\alpha = 2$. This kind of noise is often called rate random walk when appears in rate gyros, or acceleration random walk if it appears in accelerometers. To avoid confusion, from now on it will be called rate random walk (RRW).

The state space representation of a pure RRW is:

$$\begin{cases} \dot{z}_K(t) &= \omega_K(t) \qquad \text{State Equation} \\ z(t) &= z_K(t) \qquad \text{Output Equation} \end{cases} \tag{1.9}$$

where $z_K(t)$ is the contribution of the RRW to the total noise $z(t)$ and $\omega_K(t)$ is a driving white Gaussian noise with PSD $Q_K = K^2$. The state space matrices are: $A = 0$, $B = 1$, $C = 1$, $D = 0$.

The PSD $S_K(f)$ of this process is easily obtained considering that the transfer function $H(s)$ of the system is $H(s) = 1/s$:

$$S_K(f) = K^2 H(j2\pi f)H(-j2\pi f) = \frac{K^2}{(2\pi f)^2}. \tag{1.10}$$

Indeed, as previously mentioned, this kind of noise has power law coefficient $\alpha = 2$. By substituting $S_K(f)$ in the transformation (1.3) and computing the square root, one obtains the ADEV [1]:

$$\sigma(\tau) = \frac{K}{\sqrt{3}}\sqrt{\tau}. \tag{1.11}$$

Therefore the ADEV plot of a pure RRW is a straight line with slope 1/2. An example is given in Figure 1.6. The coefficient K can be read on the ADEV plot, even if other noises are present, by first finding a region which resembles a straight line with slope 1/2, and then continuing such line until it reaches $\tau = 3$. The value of the ADEV in this point is the value of the coefficient K.

As for the ARW, sometimes regions of the plot having slope +1/2 may not actually represent the RRW. This is better explained when discussing the next noise, the bias instability.

Bias instability (flicker noise) and Gauss-Markov first order process

The bias instability, also called flicker noise or random flickering, is a low-frequency noise generated by the flickering in the electronic components of the IMU.

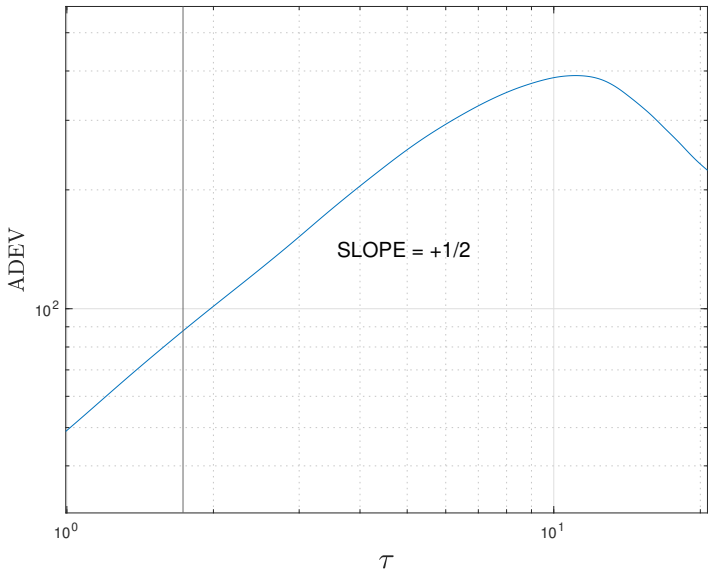

Figure 1.6: Example of an ADEV plot for a random walk frequency noise. A vertical line corresponding to $\tau = \sqrt{3}$ has been drawn, so that the noise coefficient can be easily read: $K \simeq 88$. The sudden drop for large τ is due to uncertainty in the ADEV computation.

The bias instability PSD is defined as follows (from [1]):

$$S_B(f) = \begin{cases} \frac{B^2}{2\pi}\frac{1}{f} & \text{for } f < f_0 \\ 0 & \text{for } f > f_0 \end{cases} \tag{1.12}$$

where B is the bias instability coefficient and f_0 the cut-off frequency. The ADEV is then computed by substituting this PSD in the transformation (1.3) and taking the square root [1]:

$$\sigma(\tau) = B\Big[\frac{2}{\pi}\Big(\log 2 - \frac{\sin^3 x}{2x^2}(\sin x + 4xcos(x) + C_i(x) - C_i(x)\Big)\Big]^{1/2} \tag{1.13}$$

where $x = \pi f_0 \tau$ and C_i is the Cosine Integral function:

$$C_i(x) = -\int_x^{+\infty} \frac{\cos t}{t}\, dt. \tag{1.14}$$

The ADEV plot presents a straight line with slope +1 for $\tau < \frac{1}{f_0}$. For $\tau > \frac{1}{f_0}$, the terms in equation (1.13) containing x becomes small and the ADEV can be written as:

$$\sigma(\tau) \simeq B\sqrt{\frac{2\log 2}{\pi}} = 0.664B \tag{1.15}$$

which is a straight line with slope 0. The resulting plot is shown in Figure 1.7, from [1]. The coefficient B can be estimated by dividing the value of the ADEV in the zero-slope region by 0.664.

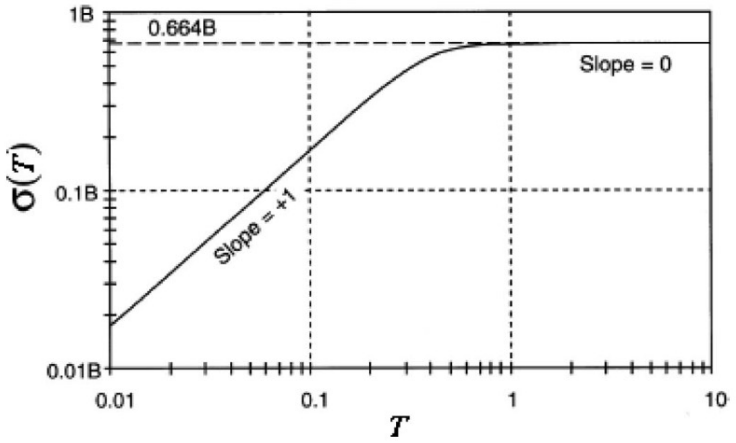

Figure 1.7: Ideal ADEV plot for bias instability noise, from [1]. The T is for time.

In IMU analysis, Bias instability is used to represent the contribution given by the part of the ADEV with slope = 0. Indeed, being ARW and quantization noises almost always present in IMU systems, the region of the bias instability ADEV plot with slope +1 is usually negligible because as time goes to zero such contribution becomes less and less important, while ARW and quantization grow.

Even though the bias instability as just depicted is a useful tool, it comes with a downside: its PSD cannot be related to any transfer function $H(s)$ of a state space representation, because it is not an even function of f.

A valid approximation for the bias instability is the Gauss-Markov First Order Process (GM Process), consisting in the following equation:

$$\dot{z}_B(t) = -\frac{1}{T_B} z_B(t) + \omega_B(t) \tag{1.16}$$

where $z_B(t)$ is the approximation of the bias instability noise, T_B is the correlation time and $\omega_B(t)$ is a driving white Gaussian noise with PSD Q_B.

Its contribution to the total noise $z(t)$ is $z_B(t)$, and therefore the state space representation is:

$$\begin{cases} \dot{z}_B(t) &= -\frac{1}{T_B} z_B(t) + \omega_B(t) & \text{State Equation} \\ z(t) &= z_B(t) & \text{Output Equation} \end{cases} \tag{1.17}$$

The state space matrices are $A = -1/T_B$, $B = 1$, $C = 1$ and $D = 0$.

The transfer function $H(s)$ of the GM process is:

$$H(s) = \frac{1}{s + 1/T_B} \tag{1.18}$$

Hence the PSD:

$$S_B(f) = Q_B H(j2\pi f)H(-j2\pi f) = \frac{Q_B}{(1/T_B)^2 + (2\pi f)^2} \tag{1.19}$$

The ADEV of the GM process is obtained substituting the PSD in equation (1.3) and taking the square root. As reported at page 92 of [6], it yields:

$$\sigma(\tau) = T_B \left[\frac{Q_B}{\tau} \left(1 - \frac{T_B}{2\tau} \left(3 - 4e^{-\frac{\tau}{T_B}} + e^{-\frac{2\tau}{T_B}} \right) \right) \right]^{1/2}. \tag{1.20}$$

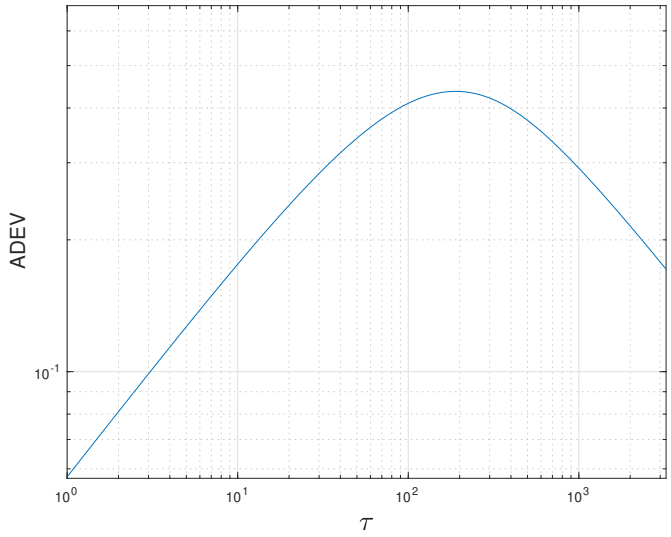

Figure 1.8: ADEV plot for Gauss-Markov First Order Process with $Q_B = 0.01$ and $T_B = 100$.

An example of GM Process ADEV plot with $Q_B = 0.01$ and $T_B = 100$ is shown in Figure 1.8. This plot presents some interesting aspects and it is a valuable aid to construct the dummy ADEV.

The curve can be split into three regions. The first one, for $\tau \ll T_B$, can be approximated as $\sigma(\tau) = \sqrt{Q_B \tau / 3}$, while the last one, for $\tau \gg T_B$, can be approximated as $\sigma(\tau) = T_B \sqrt{Q_B / \tau}$. A key aspect is that this process has always and ADEV plot characterized by two asymptotes with slope +1/2 and -1/2 respectively, regardless of the values of T_B and Q_B.

In the middle region, for $\tau \simeq 1.89 T_B$, the ADEV equation is simplified to $\sigma(\tau \simeq T_B) \simeq 0.4365 \sqrt{Q_B T_B}$.

The GM process is a very convenient model for two reasons. The first one, as already discussed, is the fact that it provides a model for the bias instability in IMU analysis which can be described by a LTI state space representation. One

can set T_B such that $1.89T_B$ is the value of τ which lies in the middle of the ADEV region with slope equal to zero, and then tune the value of Q_B to make the dummy ADEV better follow the shape of the original ADEV. An example is provided in Section 1.2.3.

The second reason is related to AVAR analysis involving other kinds of system, like the Visual Odometry System.

Consider the ADEV plot in Figure 1.8. This plot has two asymptotes: one with slope $+1/2$ for low values of τ, and one with slope $-1/2$ for high values of τ. One could think of describing the plot as the sum of ARW (ADEV slope $-1/2$) and RRW (ADEV slope $+1/2$), and applying the previously presented methods to find the coefficients N and K. This approach however is incorrect, as it leads to a reconstructed ADEV which is very different from the original one. Indeed, by looking at the region of Figure 1.8 where the plot resembles a line with slope $-1/2$ (large values of τ), to find the ARW coefficient N one could prolong the tangent line with slope $-1/2$ until it reaches $\tau = 1$. The ADEV value in this point is about 5, so the ARW coefficient would be $N = 5$.

One could follow then the same approach to find the RRW coefficient K: the first region of the plot (resembling a straight line with slope $1/2$) for $\tau = \sqrt{3}$ reaches a value of about 0.075, so the RRW coefficient would be $K = 0.075$.

A dummy ADEV constructed with these values of N and K is shown in Figure 1.9.

The two plots are totally different. This happens because ARW and RRW noises can't reconstruct an ADEV with a concave general trend (which is, with a second derivative with respect to τ negative almost everywhere). This becomes trivial considering these noises in terms of τ: as τ becomes smaller, the ARW grows while the RRW decreases, so below a certain τ the ADEV can only have negative slope. The opposite is true for large values of τ: over a certain point of the τ-axis, if the noises in the signal are just ARW and RRW, the latter is for sure the dominant one, and the ADEV can only increase.

The GM process solves in part this issue: being its ADEV a parabola-like concave shape, it can be used to reconstruct the ADEV of signals having regions characterized by a concave trend. This behaviour is extremely useful in the AVAR analysis.

The problem is solved "in part" because the GM process ADEV presents always two asymptotes with slope $+1/2$ and $-1/2$. If the original ADEV has, in the given range of τ, a parabola-like concave shape with "softer" slopes (for example, $1/10$ and $-1/10$), such ADEV can be reconstructed with the right combination of GM process and low ARW and RRW.

On the contrary, if the slopes are larger than $+1/2$ and $-1/2$ (for example $+1$ and -1), the parabola of the original ADEV will be too tight to be correctly described by any sum of these fundamental noises. If this is the case, one can keep using this process taking into account the related accuracy issues - as in the $50Hz$ DGPS Analysis in [8] - or introduce higher order processes and their AVAR.

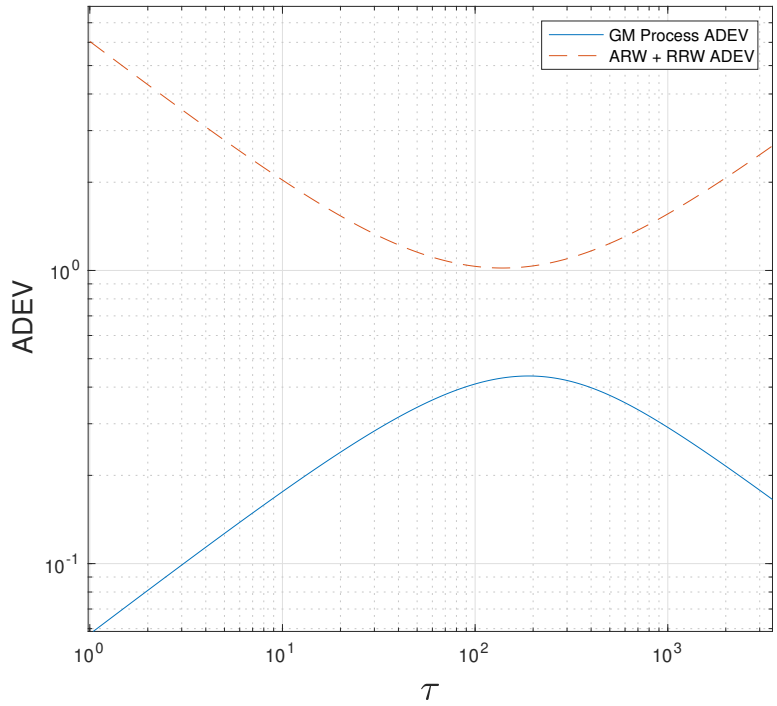

Figure 1.9: ADEV of a GM process compared to a Dummy ADEV of ARW and RRW noises.

Unfortunately, the literature on this topic is quite scarse.

Furthermore, as an inverse formula for the transformation PSD-ADEV (1.3) is not available, it is hard to "reverse-engineer" a PSD starting from a particular ADEV curve, and one cannot be sure that once obtained a PSD it actually leads to a linear state space representation.

Drift rate ramp - Flicker walk FM

The drift rate ramp and the flicker walk FM have different nature but present the same PSD, and therefore the same ADEV.

The flicker walk FM, or flicker FM, is an ideal noise defined by its own PSD, while the drift rate ramp is often the result of deterministic errors in IMUs (see [1]). Here, to avoid confusion, the noise associated with this PSD will be called just drift rate ramp, or rate ramp. It is described by the power law with $\alpha = 3$:

$$S_R(f) = \frac{R^2}{(2\pi f)^3}. \tag{1.21}$$

Being $S_R(f)$ an odd function of f, the rate ramp, as the bias instability, is not related to any state space representation.

The resulting ADEV, considering the equation (1.3), is [1]:

$$\sigma(\tau) = \frac{R\tau}{\sqrt{2}}. \tag{1.22}$$

The resulting ADEV plot is a straight line with slope +1, and the coefficient R can be found by checking the value of the ADEV for $\tau = \sqrt{2}$.

An example of ADEV plot for rate ramp noise with $R = 1$ is given in Figure 1.10.

1.2.3 Example of ADEV analysis with ARW, RRW and bias instability

In this section, starting from a given ADEV curve, the coefficients for ARW, RRW and bias instability - approximated by a GM Process - are obtained.

All the plots will have x-axis described in terms of time instead of τ, because in this example the sampling frequency is not equal to $1Hz$. Indeed, as explained at the end of Section 1.1.1, the time axis and the τ-axis are equivalent only if the sampling frequency is $1Hz$.

Consider the ADEV plot in Figure 1.11. There is a first region, for $t < 0.1$, which resembles a straight decreasing line. By plotting a dummy ADEV with just pure ARW, one can check if this region has slope -1/2. To plot such curve in a log-log plot, the needed function of t is $f_{ARW}(t) = \bar{N}/\sqrt{t}$, where $\bar{N}$ is the ARW coefficient of the dummy ADEV. At the moment, $\bar{N}$ is just a number arbitrarily chosen to position the dummy ADEV near the region of interest.

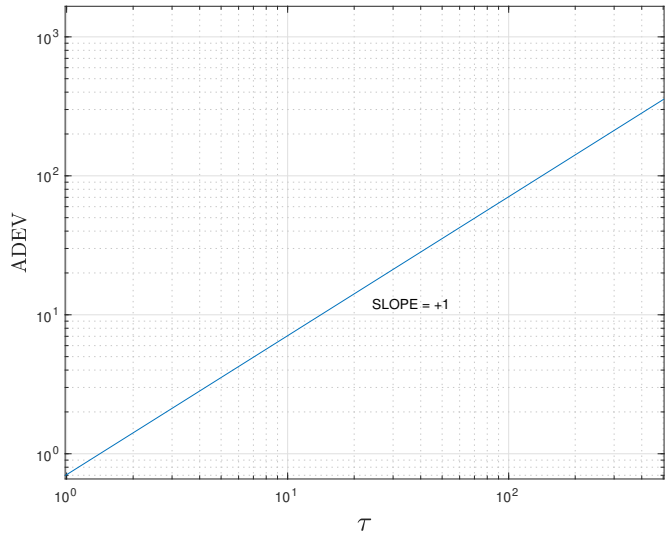

Figure 1.10: Example of an ADEV plot for rate ramp noise with $R = 1$.

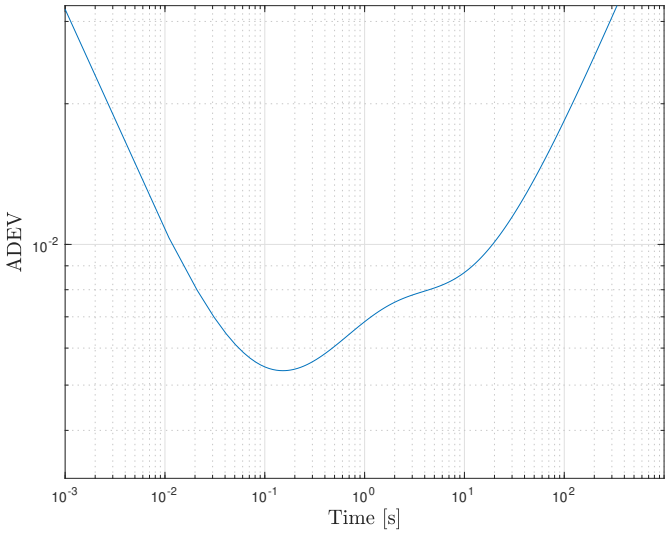

Figure 1.11: Example of an ADEV plot.

Another region worthy of notice is for $t > 3$, which may resemble a straight line with slope $+1/2$. To check if this is true, one can plot a straight line having said slope. In this case, the function that has to be plotted is $f_{RRW}(t) = \bar{K}\sqrt{\frac{t}{3}}$ where $\bar{K}$ is the RRW coefficient of the dummy ADEV. The division by 3 in the square root is introduced because, as one can check by looking at (1.11), without this factor the obtained coefficient $\bar{K}$ would be the RRW coefficient times $\sqrt{3}$. The plot of these two dummy ADEVs is shown in Figure 1.12. The two lines are indeed parallel to the original ADEV in the given ranges of t.

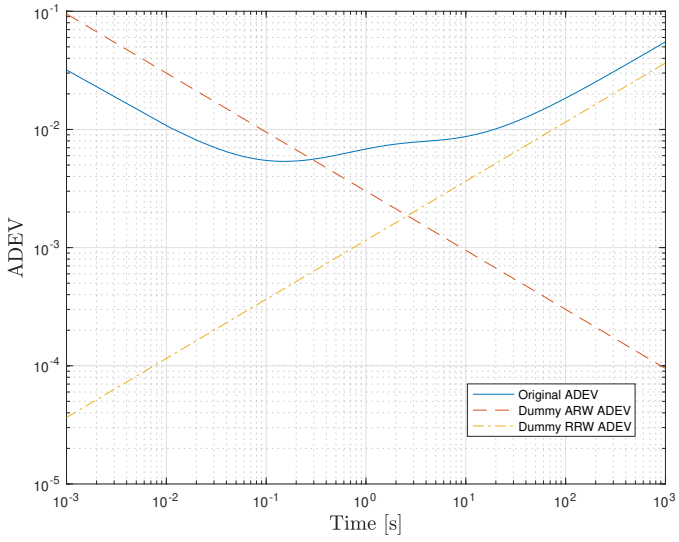

Figure 1.12: Example of an ADEV plot with two dummy ADEVs for ARW and RRW.

Once it is sure that these regions represent ARW and RRW noises, a first guess for $\bar{N}$ and $\bar{K}$ can be made "manually" by prolonging the lines tangent to the original ADEV, as shown in the left plot of Figure 1.13. Then, one has just to check the values they reach for, respectively, $t = 1$ and $t = \sqrt{3}$.

Once the first guesses are available, one has to tune them in such a way that the two dummy lines overlap as accurately as possible the original ADEV. The results obtained are $\bar{N} = 0.001$ and $\bar{K} = 0.003$. Sometimes, if other noises are required to construct the dummy ADEV, one may have to re-tune these values after adding the other noises, an go on iteratively until the desired shape is achieved.

In the right plot of Figure 1.13, the sum of these two dummy ADEVs is shown. The outer regions of the original ADEV are well approximated by the dummy, while the middle region is not. One can see that the middle region contains a sort of "bump", which might be described by a GM process. A possible first guess for the value of t where the parabola-like shape of the GM process ADEV may reach the maximum is $t = 2$. This means that a possible T_B could be, as explained when

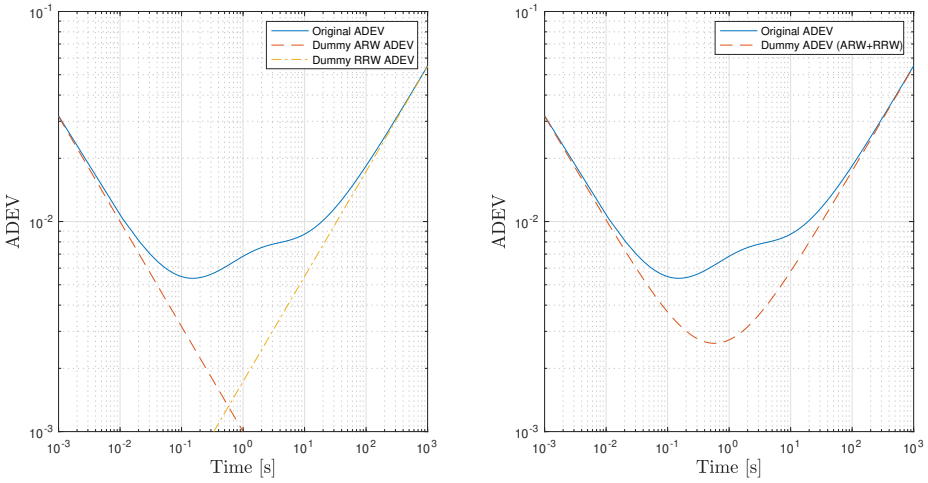

Figure 1.13: Example of an ADEV with two dummy ADEVs for ARW and RRW (left plot) and their sum (right plot).

discussing the GM process, $\bar{T}_B = 2/1.89 = 1.0582$. For $t = 2$, the original ADEV is equal to about $\sigma(2) = 0.0075$, and considering that $\sigma(2) \simeq 0.4354\sqrt{\bar{Q}_B \bar{T}_B}$ a first guess for the coefficient $\bar{Q}_B$ is:

$$\bar{Q}_B = \left(\frac{\sigma(2)}{0.4354}\right)^2 \frac{1}{\bar{T}_B} = \left(\frac{0.0075}{0.4354}\right)^2 \frac{1}{1.0582} = 2.804 \cdot 10^{-4} \tag{1.23}$$

Once the first guesses for $\bar{T}_B$ and $\bar{Q}_B$ have been found, one can plot the dummy ADEV of the GM process by substituting these values in equation (1.20). The obtained curve is shown in the left plot of Figure 1.14.

The total dummy ADEV, considering all the contributions (ARW+RRW+GM), is shown in the right plot of Figure 1.14. The dummy ADEV is quite similar to the original, but further tuning of the coefficients $\bar{T}_B$ and $\bar{Q}_B$ is required. As rule of thumb, one can remember that variations of $\bar{Q}_B$ control the altitude of the dummy ADEV of the GM process, while small variations of $\bar{T}_B$ control only the positioning of the pseudo-parabola along the t axis.

Once the correct shape has been achieved, the obtained values of $\bar{N}$, $\bar{K}$, $\bar{T}_B$ and $\bar{Q}_B$ are the estimated coefficients of the original ADEV. In this example, the coefficients of the Original ADEV were $N = 0.001$, $K = 0.003$, $T_B = 1$, $Q_B = 0.0001$.

One should be aware of a couple of issues while performing this kind of analysis. Consider the ADEV, generated from real data, shown in Figure 1.15. The dummy ADEV has been constructed by a sum of ARW+RRW+GM noises. The GM noise has been used to better shape the region at low values of t, where the ADEV reaches its minimum.

For large values of t, the dummy ADEV differs significantly from the original

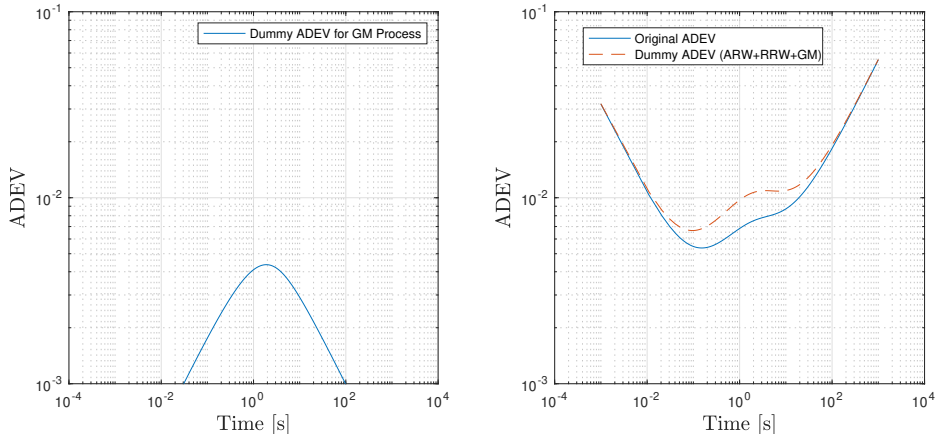

Figure 1.14: Example of dummy ADEV for a GM process (left plot) and its sum with dummy ADEVs for ARW and RRW (right plot).

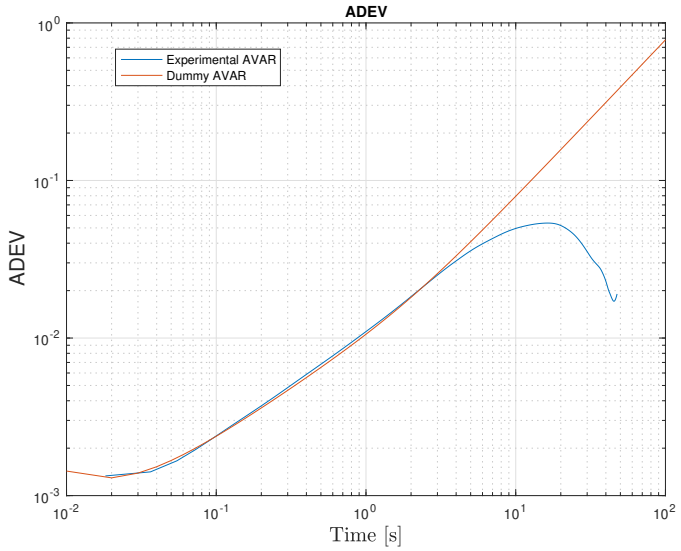

Figure 1.15: Example of ADEV and Dummy ADEV from real data.

one. This should not be a matter of concern because, as previously explained, the last part of the ADEV is characterized by a great uncertainty. Most of the times, the rightmost part of the plot presents sudden drops or oscillations, which should not be taken in account.

A second issue is related to this kind of plots, which present a region of leveling for small values of t. In this case, even if the original ADEV has no region resembling a straight line with slope -1/2, one can introduce in the dummy ADEV a very low ARW in order to better follow the curvature. This is useful especially when the right shape cannot be achieved by means of just RRW and GM noises.

1.2.4 PSD and state space representation with ARW, RRW and GM process

Once the noise coefficients are known, the total PSD of the noise and the final state space representation can be written by assembling the single contributions from all the noises.

The total PSD is just the sum of all the PSD of the considered processes:

$$S_{tot}(f) = N^2 + \frac{K^2}{(2\pi f)^2} + \frac{Q_B}{(1/T_B)^2 + (2\pi f)^2} + \frac{R^2}{(2\pi f)^3} \tag{1.24}$$

where the contributions are, respectively: ARW, RRW, GM Process, rate ramp.

To construct the state space representation, a direct formulation can be achieved only if the noises used to draw the dummy ADEV have PSDs even function of f. These noises are ARW, RRW and GM process. If other noises have been used, such as the rate ramp, there is not a readily available state space representation, and one should apply approximation method starting from the total PSD obtained.

Here are briefly recalled the contributions of the different noises to the dynamic system (1.4):

- ARW: this noise appears only in the output equation for the total noise $z(t)$ as a forcing term (direct transmission term). Its contribution is $z_N(t) = \omega_N$ where ω_N is a white Gaussian noise with PSD $Q_N = N^2$.

- RRW: its contribution to the total noise is $z_K(t)$, and its dynamics are described by the equation $\dot{z}_K = \omega_K$, where ω_K is a white Gaussian noise with PSD $Q_K = K^2$.

- GM Process: its contribution to the total noise is $z_B(t)$ and its dynamics are described by the equation $\dot{z}_B = -\frac{1}{T_B} z_B + \omega_B$ where ω_B is a white Gaussian noise with PSD Q_B.

The final state space representation, in continuous time, is therefore:

$$\begin{Bmatrix} \dot{z}_B \\ \dot{z_K} \end{Bmatrix} = \begin{bmatrix} -\frac{1}{T_B} & 0 \\ 0 & 0 \end{bmatrix} \begin{Bmatrix} z_B \\ z_K \end{Bmatrix} + \begin{bmatrix} 1 & 0 \\ 0 & 1 \end{bmatrix} \begin{Bmatrix} \omega_B \\ \omega_K \end{Bmatrix} \tag{1.25}$$

$$z = \begin{bmatrix} 1 & 1 \end{bmatrix} \begin{Bmatrix} z_B \\ z_K \end{Bmatrix} + \omega_N \tag{1.26}$$

With the continuous time process noise PSD matrix Q:

$$Q = \begin{bmatrix} Q_B & 0 \\ 0 & K^2 \end{bmatrix} \tag{1.27}$$

1.2.5 ADEV approximation for states-space-based analysis

Depending on the nature of the system, the degrees of freedom given by ARW, RRW and Gaus-Markov process noises might not be enough to properly construct the dummy ADEV. If this is the case, one should decide if it is convenient to introduce other noises besides those.

This choice depends essentially on two factors: the quality of the PSD obtained from the dummy ADEV, and the kind of analysis one desires to perform. Indeed, if the state space representation is required - for example, as in this thesis, it might be used to construct a Kalman predictor to validate the results - then there are two options available.

The first one - as previously mentioned - is to use all the needed noises to construct the dummy ADEV, and then, once the total PSD is obtained, one can apply approximation methods to obtain a state space representation. This approach can lead to better results, but it is also more time consuming.

The second option is to accept a stronger approximation and construct the dummy ADEV just by considering the noises ARW, RRW, and GM.

To understand if this second approach is valid, one can apply the following method: construct two different dummy ADEV, one with only the three mentioned noises and the other with all the noises required to make it fit the best. Then, once the noise coefficients are known, plot and compare their PSD, considering in which range of frequency the system will operate.

For example, consider Figures 1.16 and 1.17.

The experimental ADEV is the same in both plots, while in Figure 1.16 the dummy ADEV is constructed with only ARW, RRW and GM noises ($N = 1e-5$, $K = 0.009$, $Q_B = 2.5e-5$, $T_B = 7$) and in Figure 1.17 it is constructed considering also Rate Ramp Noise ($N = 2.2e-4$, $K = 0.0018$, $Q_B = 2e-5$, $T_B = 7$, $R = 0.0065$).

As one can clearly see, the introduction of Rate Ramp noise gives a strong benefit. To understand how much this difference is important in terms of perfor-

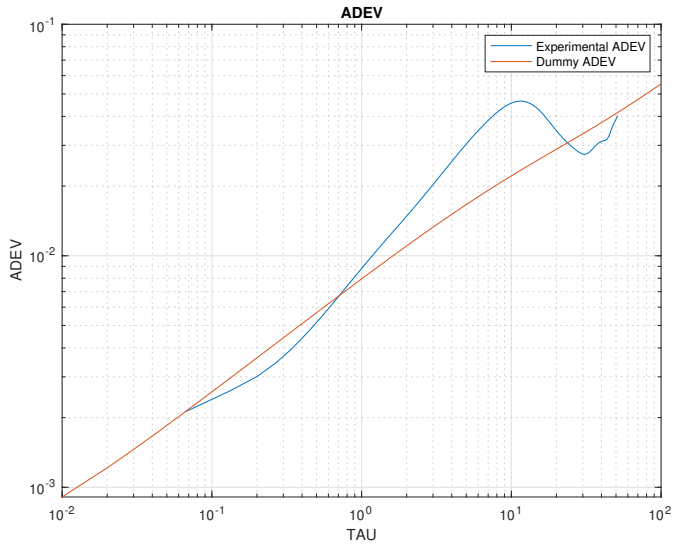

Figure 1.16: Example of ADEV and Dummy ADEV without Rate Ramp.

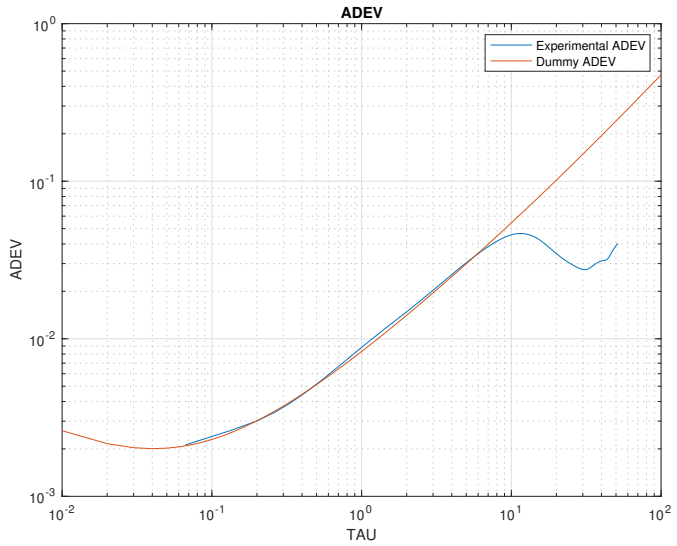

Figure 1.17: Example of ADEV and Dummy ADEV with Rate Ramp.

mance of the model, one can compare the two associated PSD. Their are shown in Figure 1.18. In the plot is also shown the characteristic frequency of acquisition of the visual odometry system of a drone (15Hz), which will be the system studied in the next chapter. In this case, one can see that the difference in terms of ARW - which for the PSD with Rate Ramp is the dominant one after 10 Hz - is the main source of error. This is due to the fact that it is difficult to find the right value of N without having the dummy ADEV fit properly for high values of τ. If the Rate Ramp is introduced, the possible range of N becomes very small.

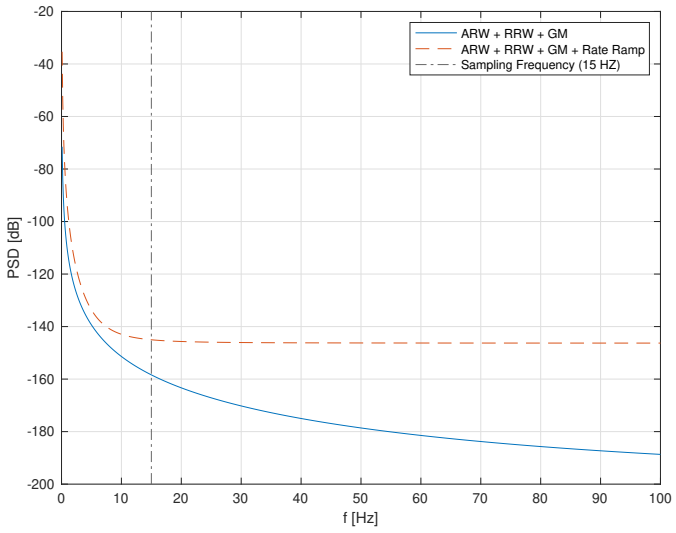

Figure 1.18: Comparison between PSD with and without Rate Ramp noise.

Chapter 2

Visual odometry system noise analysis

In this chapter, the methodology of the experiments and the results of the AVAR-based analysis of the noise acting on a drone's visual odometry system are presented.

The results are then compared to investigate how different choices of some parameters can change the dynamics of the noise.

Lastly, the time-continuous model of the noise is discretized and a Kalman predictor is constructed in order to compare the noise model obtained from the analysis with the real measured noise. The chapter ends with an example of application of the predictor.

2.1 Visual odometry

Visual Odometry (VO) is a technique consisting in the estimation of a body's motion through the process of analyzing and comparing subsequent pictures taken from a camera mounted on the body itself. If the system mounts a single camera, the technique is called Monocular VO, while if the cameras are two (stereoscopic vision) it is called Stereo VO.

As showed in [9], the VO implementation can be conceptualized as follows. Consider two consequent poses of the cameras, P_i and P_{i+1}. These matrices represent, respectively for time instants t_i and t_{i+1}, the transformations from the fixed ground coordinate frame to the pose in cameras' coordinate frame, which is usually centered in one of the two cameras. Two subsequent poses P_i and P_{i+1} are related by the transformation T_i, represented by the matrix:

$$T_i = \begin{bmatrix} Q_{i\{3x3\}} & t_{i\{3x1\}} \\ \mathbf{0}_{\{1x3\}} & 1 \end{bmatrix} \tag{2.1}$$

where Q_i is a rotation matrix and t_i a translation vector.

The VO problem consists in the estimation, at each instant i, of the matrix T_i by means of picture comparison. There are many approaches to estimate this transformation. The methods are usually divided in Feature-Based Methods, which extract patterns of points from the images and track them in time, and Direct Methods which consider all the pixel in the images and evaluate the change of intensity from picture to picture. More details can be found in [9].

2.2 Experimental setup

2.2.1 Drone

The drone used in the experiments, called ROG-1 (Figure 2.1), is a prototype constructed by students of Politecnico di Milano which was designed and built in the framework of the Leonardo Drone Contest. Its main characteristics are here reported:

- Weight: 3.75kg
- Size: 50x50x35cm
- Electric motors: KDE2315XF-965
- 8 propellers
- Battery: LiPo 16000 mAh

Figure 2.1: ROG-1 drone.

2.2.2 Environment

All the experiments were performed indoor, in a 12m x 6m x 4m flight space, inside the FlyART laboratory of Politecnico di Milano ASCL - Aerospace Systems & Control Laboratory (Figure 2.2).

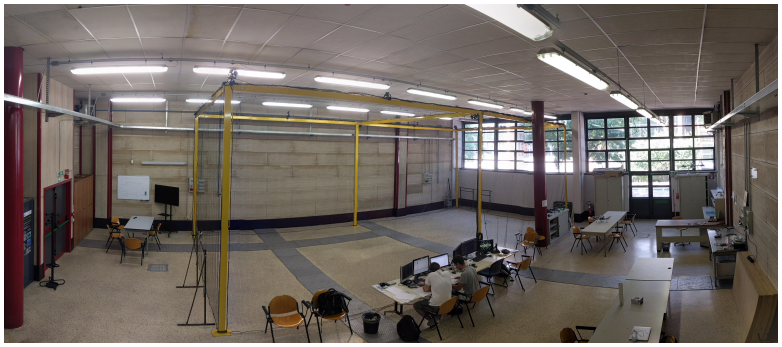

Figure 2.2: Politecnico di Milano ASCL FlyART Laboratory.

2.2.3 Visual odometry system

To perform the Stereo VO in the experiments, a Stereolabs ZED [10] stereoscopic camera (Figure 2.3) has been rigidly attached to the drone. It automatically processes the images and provides the results in terms of Cartesian coordinates for the position. During the experiments, the sampling frequency oscillated around 14-15 Hz. To perform the AVAR computations, the frequency considered is 15 Hz.

Figure 2.3: ZED stereoscopic camera.

2.2.4 Motion capture system

To compare the ZED data to true position, the motion of the drone has been tracked by a Motion Capture (MOCAP) system. The MOCAP hardware consists of eight OptiTrack Prime 13 cameras [11], connected to a desktop PC. The MOCAP software is OptiTrack Motive Tracker. The sampling frequency of the system was higher than the ZED's, therefore an undersampling process has been performed in order to obtain position vectors from the MOCAP having the same length as the ones from the ZED camera.

2.3 Description of the experiments

The reference frame, valid both for the ZED camera and the MOCAP system, is centered in the point (0,0,0) and is described by the axes East, North and Up.

Sixteen different experiments were carried out. The requested trajectory consisted in these phases:

1. take-off from point (0,0,0) and vertical ascent up to a certain altitude h
2. following a straight line from point $(0, 0, h)$ to point $(0, 1, h)$
3. following for a given number of times a circular path with radius $1m$ centered in Up axis, maintaining the altitude h. The last circle ends in point $(0, 1, h)$
4. following a straight line from point $(0, 1, h)$ to point $(0, 0, h)$
5. vertical descent and landing in point $(0, 0, 0)$.

An example of a real trajectory - with three full circles - followed by the drone is shown in Figure 2.4.

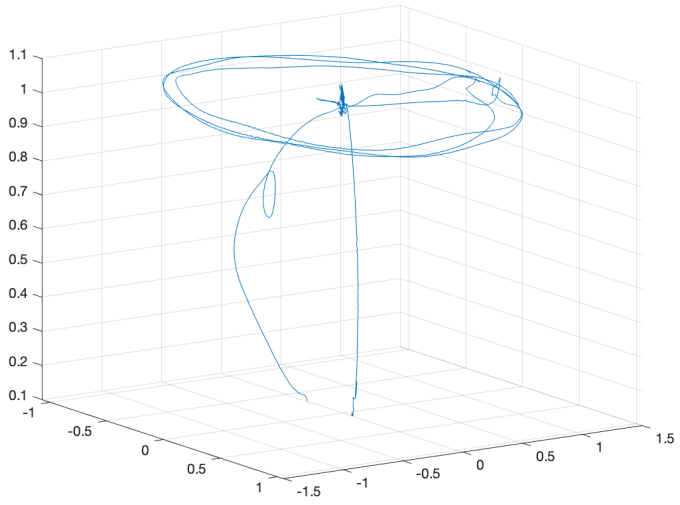

Figure 2.4: Example of real trajectory from one of the experiments.

Each experiment was defined by a different choice of the following factors:

- Height h: two possible heights were considered, $h = 1m$ and $h = 2m$.
- Trajectory angular velocity (TAV): two different values of the angular speed, maintained by the drone's center of mass about axis Up during the circular

Table 2.1: Summary of the experiments

Run	1	2	3	4	5	6	7	8	9	10	11	12	13	14	15	16
Height [m]	1	2	1	2	1	2	1	2	1	2	1	2	1	2	1	2
TAV [rad/s]	0.2	0.2	0.6	0.6	0.2	0.2	0.6	0.6	0.2	0.2	0.6	0.6	0.2	0.2	0.6	0.6
YF	N	N	N	N	Y	Y	Y	Y	N	N	N	N	Y	Y	Y	Y
Light [lux]	100	100	100	100	100	100	100	100	250	250	250	250	250	250	250	250

path, have been considered: 0.2 rad/s and 0.6 rad/s. To have comparable time lengths between the experiments, if the chosen speed was 0.2 rad/s the drone completed a single circle, while, if the chosen speed was 0.6 rad/s, the drone completed 3 circles.

- Yaw following (YF) inactive or active (N/Y): when the yaw following mode is active, the drone's attitude is adjusted in each point of the trajectory in such a way that a chosen body axis always points in the direction of the velocity vector. If this mode is inactive, the drone points always in the same direction in every point of the trajectory.

- Average light: neon lamps were positioned in the environment to control the light conditions. Two different light intensities were considered: 100 lux and 250 lux. The light was measured with a smartphone app.

The experiments are summarized in Table 2.1.

In all the experiments, the dummy ADEV has been constructed only with ARW, RRW and GM process noises.

Table 2.2: ARW coefficient N for the different experiments

Run	1	2	3	4	5	6	7	8	9	10	11	12	13	14	15	16
Height [m]	1	2	1	2	1	2	1	2	1	2	1	2	1	2	1	2
TAV [rad/s]	0.2	0.2	0.6	0.6	0.2	0.2	0.6	0.6	0.2	0.2	0.6	0.6	0.2	0.2	0.6	0.6
YF	N	N	N	N	Y	Y	Y	Y	N	N	N	N	Y	Y	Y	Y
Light [lux]	100	100	100	100	100	100	100	100	250	250	250	250	250	250	250	250
N - East	6E-05	1E-04	5E-05	3E-05	1.1E-4	1E-04	1.8e-4	1E-04	7E-05	1.3e-4	2E-04	1E-04	1.5e-4	1.4e-4	1.4e-4	1.4e-4
N - North	7E-05	1E-04	1E-04	1E-04	1.5e-4	1E-04	1.4e-4	1.4e-4	1E-04	1.4e-4	2E-04	0	2E-03	0	1E-04	0
N - Up	5E-05	1E-04	0	1E-05	1E-05	1.8e-4	2.2e-4	0	1.6e-4	4E-04	5.5e-5	0	1.5e-4	0	0	0

2.4 Results of the experiments

In this section, the results of the experiments are presented in terms of noise on the position measurement. For each noise coefficient (ARW - N, RRW - K, Gauss Markov - T_B and Q_B), five comparisons have been performed: differences between the three axes (East, North, Up), differences between trajectory heights, differences between TAVs, differences between YF inactive or active, differences between environment light.

2.4.1 ARW - Coefficient N

Comparison between axes East-North-Up

In Table 2.2 the values of the coefficient N are reported for each experiment. The results for axes East and North are compared in Figure 2.5, while the results for axis Up - compared with East and North averages - are shown in Figure 2.6.

In some runs the coefficient N is zero. This is due to the ADEV sensitivity to other noises, and to the sampling interval of the system. In fact, the ARW is not zero but it can't be detected by the ADEV. These results are not shown in the plots. The value $N = 0.002$ of run 13-North is not reported as well, because it has been considered an outlier.

The maximum value of N is $N = 4e - 4$ from run 10-Up. In the experiments with non-null values of N, the values of the ARW are generally larger for the North axis with respect to the East axis. This might be due to the fact that the trajectory followed by the drone contains two straight line along the North axis, while in the ideal trajectory the drone moves along the East axis only during the circular path.

In three runs (2-6-11) the values of N for East and North are almost identical, while in run 7 only for East axis is larger.

The variance of set East is $2.5902e - 09$ while the one of the set North is $1.2182e - 09$.

Considering Figure 2.6, one can see that the average value for the Up axis is similar to the ones of the other axes, but the single values are sparser: the variance for the set Up is $1.4084e-08$.

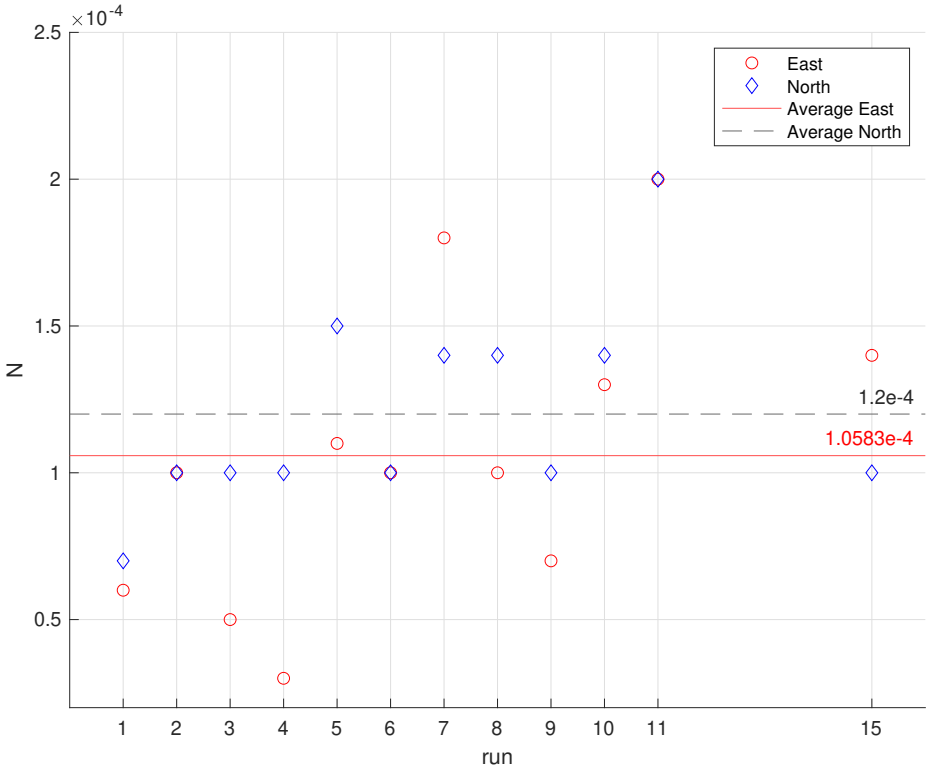

Figure 2.5: Comparison between ARW coefficients of axes East and North for the different experiments.

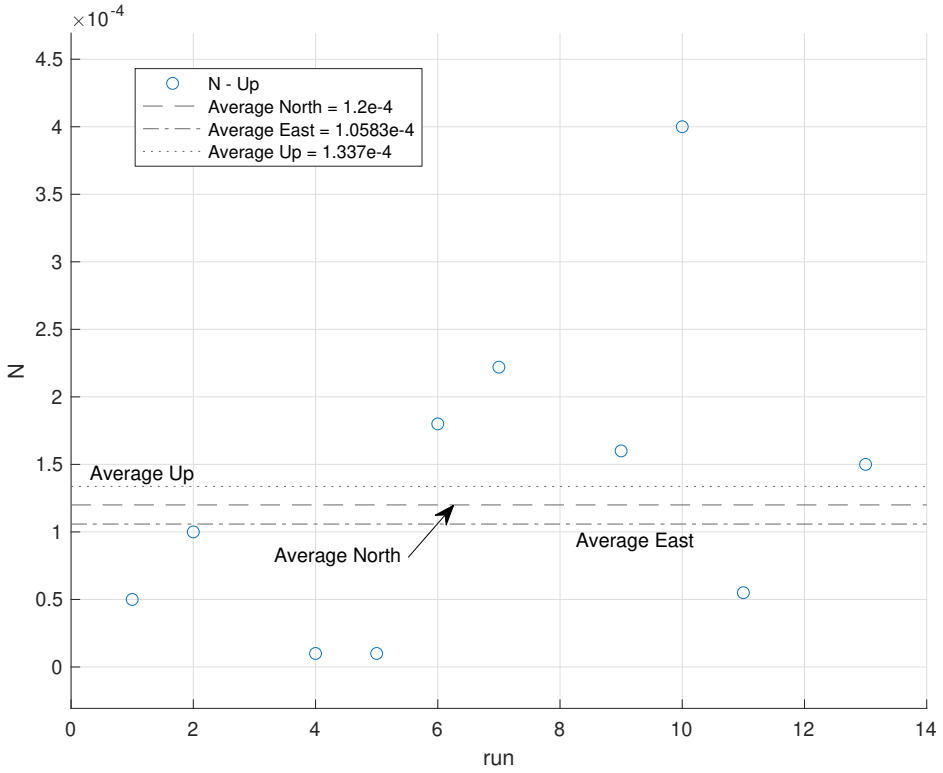

Figure 2.6: Comparison between ARW coefficients of axis Up for the different experiments.

Table 2.3: ARW coefficient N for different heights.

	TAV* = 0.2 YF: N 100 lux		TAV = 0.6 YF: N 100 lux		TAV = 0.2 YF: Y 100 lux		TAV = 0.6 YF: Y 100 lux		TAV = 0.2 YF: N 250 lux		TAV = 0.6 YF: N 250 lux		TAV = 0.2 YF: Y 250 lux		TAV = 0.6 YF: Y 250 lux	
Height:	**1m**	**2m**	**1m**	**2m**	**1m**	**2m**	**1m**	**2m**	**1m**	**2m**	**1m**	**2m**	**1m**	**2m**	**1m**	**2m**
Run	1	2	3	4	5	6	7	8	9	10	11	12	13	14	15	16
N - East	6E-05	1E-04	5E-05	3E-05	1.1E-4	1E-04	1.8E-4	1E-04	7E-05	1.3E-4	2E-04	1E-04	1.5E-4	1.4E-4	1.4E-4	1.4E-4
N - North	7E-05	1E-04	1E-04	1E-04	1.5E-4	1E-04	1.4E-4	1.4E-4	1E-04	1.4E-4	2E-04	0	2E-03	0	1E-04	0
N - Up	5E-05	1E-04	0	1E-05	1E-05	1.8E-4	2.2E-4	0	1.6E-4	4E-04	5.5E-5	0	1.5E-4	0	0	0

***TAV is in [rad/s]**

ARW - Comparison between different choices of heights

The comparison between ARW values for different choices of heights is shown in Table 2.3 and in Figure 2.7. The plot does not include the cases for $N = 0$ and the outlier $N = 0.002$ of run 13-North.

In set East, the coefficient N decreases in all the runs except for the couples r1-r2 and r9-r10, which have in common a TAV of 0.2rad/s and the Yaw Following inactive - when the height increases from 1m to 2m. Despite this, there is no evident correlation between ARW and height for East and North axes. The set Up does not contain enough points to come to a conclusion.

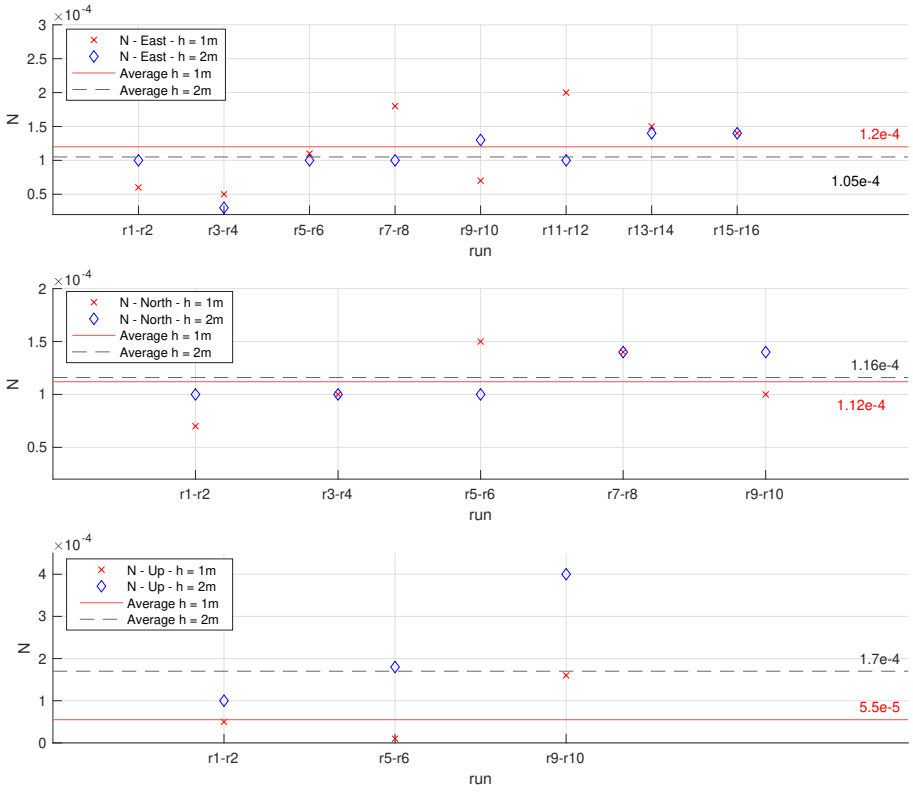

Figure 2.7: Comparison between ARW values for different heights.

Table 2.4: ARW coefficient N for different TAV.

	h = 1m 100 lux YF: N		h = 2m 100 lux YF: N		h = 1m 100 lux YF: Y		h = 2m 100 lux YF: Y		h = 1m 250 lux YF: N		h = 2m 250 lux YF: N		h = 1m 250 lux YF: Y		h = 2m 250 lux YF: Y	
TAV [rad/s]	0.2	0.6	0.2	0.6	0.2	0.6	0.2	0.6	0.2	0.6	0.2	0.6	0.2	0.6	0.2	0.6
Run	1	3	2	4	5	7	6	8	9	11	10	12	13	15	14	16
N - East	6E-05	5E-05	1E-04	3E-05	1.1E-4	1.8E-4	1E-04	1E-04	7E-05	2E-04	1.3E-4	1E-04	1.5E-4	1.4E-4	1.4E-4	1.4E-4
N - North	7E-05	1E-04	1E-04	1E-04	1.5E-4	1.4E-4	1E-04	1.4E-4	1E-04	2E-04	1.4E-4	0	2E-03	1E-04	0	0
N - Up	5E-05	0	1E-04	1E-05	1E-05	2.2E-4	1.8E-4	0	1.6E-4	5.5E-5	4E-04	0	1.5E-4	0	0	0

ARW - Comparison between different choices of TAV

The comparison between ARW values for different choices of TAV is shown in Table 2.4 and in Figure 2.8. The plot does not include the cases for $N = 0$ and the outlier $N = 0.002$ of run 13-North.

The coefficient N appears to be independent of the TAV, in all the axes: the values oscillates from run to run but no evident pattern can be recognized.

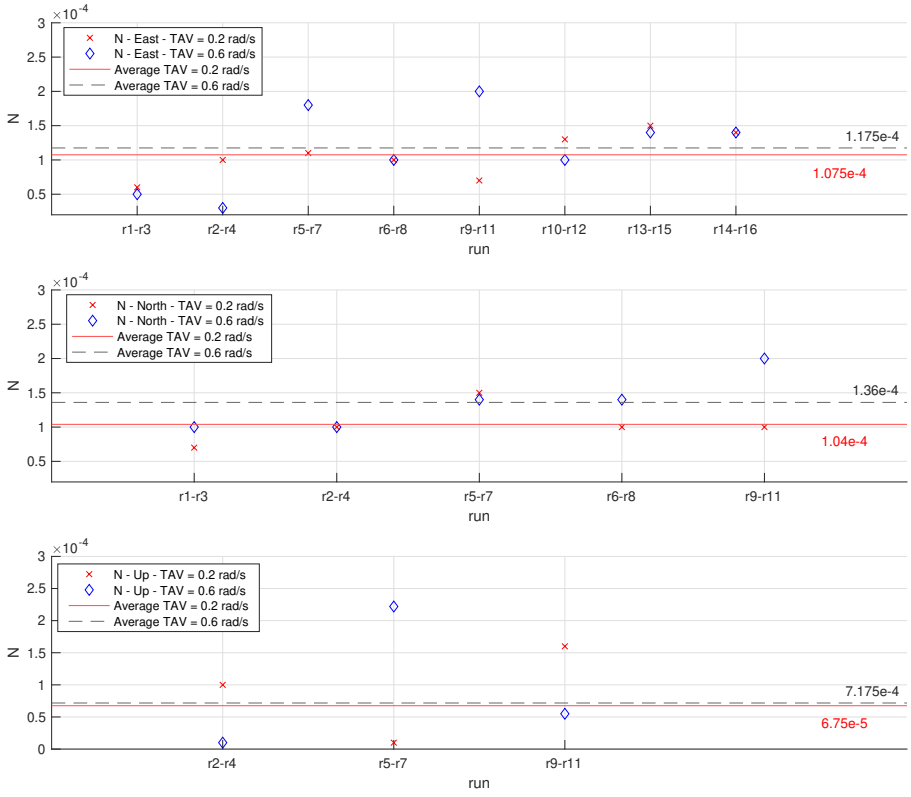

Figure 2.8: Comparison between ARW values for different TAV.

Table 2.5: ARW coefficient N with YF inactive or active.

	h = 1m TAV* = 0.2 100 lux		h = 2m TAV = 0.2 100 lux		h = 1m TAV = 0.6 100 lux		h = 2m TAV = 0.6 100 lux		h = 1m TAV = 0.2 250 lux		h = 2m TAV = 0.2 250 lux		h = 1m TAV = 0.6 250 lux		h = 2m TAV = 0.6 250 lux	
YF:	N	Y	N	Y	N	Y	N	Y	N	Y	N	Y	N	Y	N	Y
Run	1	5	2	6	3	7	4	8	9	13	10	14	11	15	12	16
N - East	6E-05	1.1E-4	1E-04	1E-04	5E-05	1.8E-4	3E-05	1E-04	7E-05	1.5E-4	1.3E-4	1.4E-4	2E-04	1.4E-4	1E-04	1.4E-4
N - North	7E-05	1.5E-4	1E-04	1E-04	1E-04	1.4E-4	1E-04	1.4E-4	1E-04	2E-03	1.4E-4	0	2E-04	1E-04	0	0
N - Up	5E-05	1E-05	1E-04	1.8E-4	0	2.2E-4	1E-05	0	1.6E-4	1.5E-4	4E-04	0	5.5E-5	0	0	0

*TAV is in [rad/s]

ARW - Comparison between runs performed with and without the Yaw Following mode

The comparison between ARW values for the Yaw Following mode inactive or active is shown in Table 2.5 and in Figure 2.9. The plot does not include the cases for $N = 0$ and the outlier $N = 0.002$ of run 13-North.

In general, for axes East and North the activation of Yaw Following mode is associated with a rise of coefficient N. Exception are the couples of runs containing $N = 0$ and the couples r11-r15 of the East axis and r2-r6 of both East and North axes (which maintains the same value). The behaviour in the Up axis is not clear, because of the little number of values available from the ADEV.

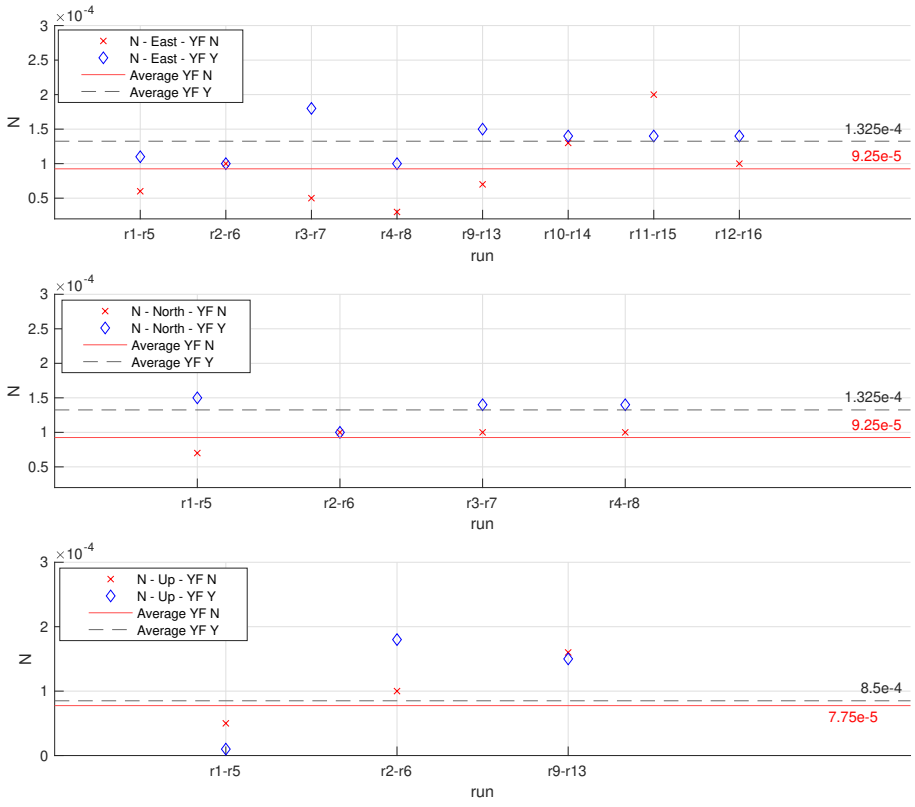

Figure 2.9: Comparison between ARW values with YF active or inactive.

Table 2.6: ARW coefficient N for different light intensities.

	h = 1m TAV* = 0.2 YF: N		h = 2m TAV = 0.2 YF: N		h = 1m TAV = 0.6 YF: N		h = 2m TAV = 0.6 YF: N		h = 1m TAV = 0.2 YF: Y		h = 2m TAV = 0.2 YF: Y		h = 1m TAV = 0.6 YF: Y		h = 2m TAV = 0.6 YF: Y	
Light [lux]	**100**	**250**	**100**	**250**	**100**	**250**	**100**	**250**	**100**	**250**	**100**	**250**	**100**	**250**	**100**	**250**
Run	1	9	2	10	3	11	4	12	5	13	6	14	7	15	8	16
N - East	6E-05	7E-05	1E-04	1.3E-4	5E-05	2E-04	3E-05	1E-04	1.1E-4	1.5E-4	1E-04	1.4E-4	1.8E-4	1.4E-4	1E-04	1.4E-4
N - North	7E-05	1E-04	1E-04	1.4E-4	1E-04	2E-04	1E-04	0	1.5E-4	2E-03	1E-04	0	1.4E-4	1E-04	1.4E-4	0
N - Up	5E-05	1.6E-4	1E-04	4E-04	0	5.5E-5	1E-05	0	1E-05	1.5E-4	1.8E-4	0	2.2E-4	0	0	0

***TAV is in [rad/s]**

ARW - Comparison between different choices of environment light intensities

The comparison between ARW values for different intensities of environmental light is shown in Table 2.6 and in Figure 2.10. The plot does not include the cases for $N = 0$ and the outlier $N = 0.002$ of run 13-North.

A rise of environmental light from 100 to 250 lux appears to be associated with an increase of ARW noise, for all the axes. This does not happen only in the comparison beetwen runs 7 and 15 - height 1m, TAV 0.6rad/s, YF active - both for East and North (this comparison for the Up axis is not available).

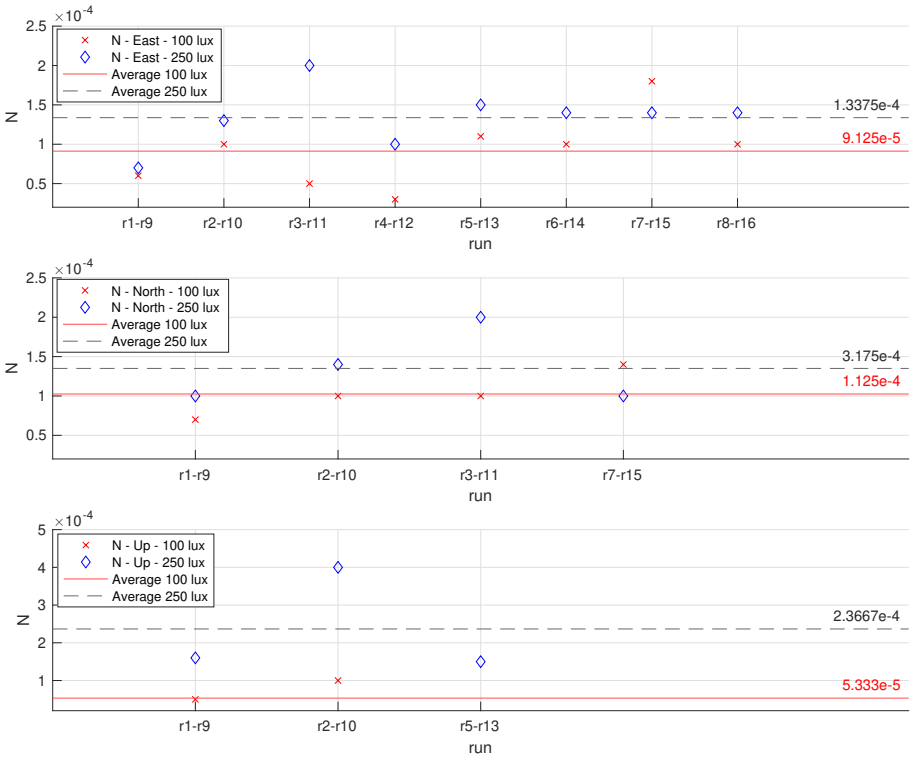

Figure 2.10: Comparison between ARW values for different environment light intensities.

Table 2.7: RRW coefficient K for the different experiments.

Run	1	2	3	4	5	6	7	8	9	10	11	12	13	14	15	16
Height [m]	1	2	1	2	1	2	1	2	1	2	1	2	1	2	1	2
TAV [rad/s]	0.2	0.2	0.6	0.6	0.2	0.2	0.6	0.6	0.2	0.2	0.6	0.6	0.2	0.2	0.6	0.6
YF	N	N	N	N	Y	Y	Y	Y	N	N	N	N	Y	Y	Y	Y
Light [lux]	100	100	100	100	100	100	100	100	250	250	250	250	250	250	250	250
K - East	0,003	0,01	0,02	0,02	0,006	0,0065	0,0095	0,02	0,005	0,0065	0,006	0,029	0,004	0,014	0,014	0,014
K - North	0,007	0,016	0,02	0,03	0,01	0,01	0,018	0,02	0,005	0,0075	0,0075	0,029	0,007	0,025	0,018	0,03
K - Up	0,007	0,015	0,015	0,027	0,01	0,01	0,013	0,03	0,0035	0,0035	0,005	0,027	0,0045	0,025	0,015	0,02

2.4.2 RRW - Coefficient K

Comparison between axes East-North-Up

In Table 2.7 the values of the coefficient K are reported for each experiment. They are compared in Figure 2.11.

Considering all the runs, the coefficient K is always contained in the interval $3e-3 < K < 3e-2$. In particular:

- East axis: $0.003 < K < 0.029$
- North axis: $0.007 < K < 0.03$
- Up axis: $0.005 < K < 0.03$

On average, the RRW affecting the East axis is smaller. This may be related to the trajectory followed by the drone, which contains two different straight paths along axes North and Up - from $(0, 0, h)$ to $(0, 1, h)$ and the vertical ascent and descent - while movements along the East axis are required only during the circular holding.

The variances of the coefficient K for the three axes are:

- East axis: 3.7856e-5
- North axis: 7.0356e-5
- Up axis: 7.5292e-5

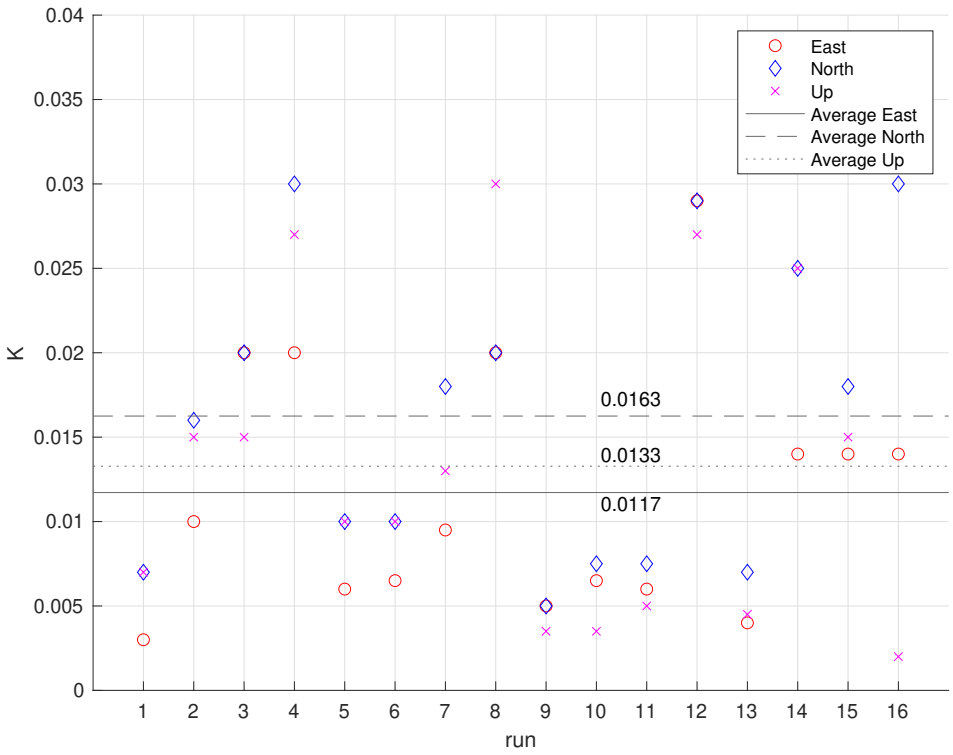

Figure 2.11: Comparison between RRW coefficients of axes East, North, Up for the different experiments.

Table 2.8: RRW coefficient N for different heights

	TAV* = 0.2 YF: N 100 lux		TAV = 0.6 YF: N 100 lux		TAV = 0.2 YF: Y 100 lux		TAV = 0.6 YF: Y 100 lux		TAV = 0.2 YF: N 250 lux		TAV = 0.6 YF: N 250 lux		TAV = 0.2 YF: Y 250 lux		TAV = 0.6 YF: Y 250 lux	
Height:	**1m | 2m**		**1m | 2m**		**1m | 2m**		**1m | 2m**		**1m | 2m**		**1m | 2m**		**1m | 2m**		**1m | 2m**	
Run	1	2	3	4	5	6	7	8	9	10	12	11	13	14	15	16
K - East	0,003	0,01	0,02	0,02	0,006	0,0065	0,0095	0,02	0,005	0,0065	0,029	0,006	0,004	0,014	0,014	0,014
K - North	0,007	0,016	0,02	0,03	0,01	0,01	0,018	0,02	0,005	0,0075	0,029	0,0075	0,007	0,025	0,018	0,03
K - Up	0,007	0,015	0,015	0,027	0,01	0,01	0,013	0,01	0,0035	0,0035	0,027	0,005	0,0045	0,025	0,015	0,02

***TAV is in [rad/s]**

RRW - Comparison between different choices of heights

The comparison between RRW values for different choices of heights is shown in Table 2.8 and in Figure 2.12.

In general, an increase of height from 1m to 2m appears to be associated with a rise of the RRW coefficient, for all the axes. In some couples of runs this variation is low, but these couples don't have characteristics in common.

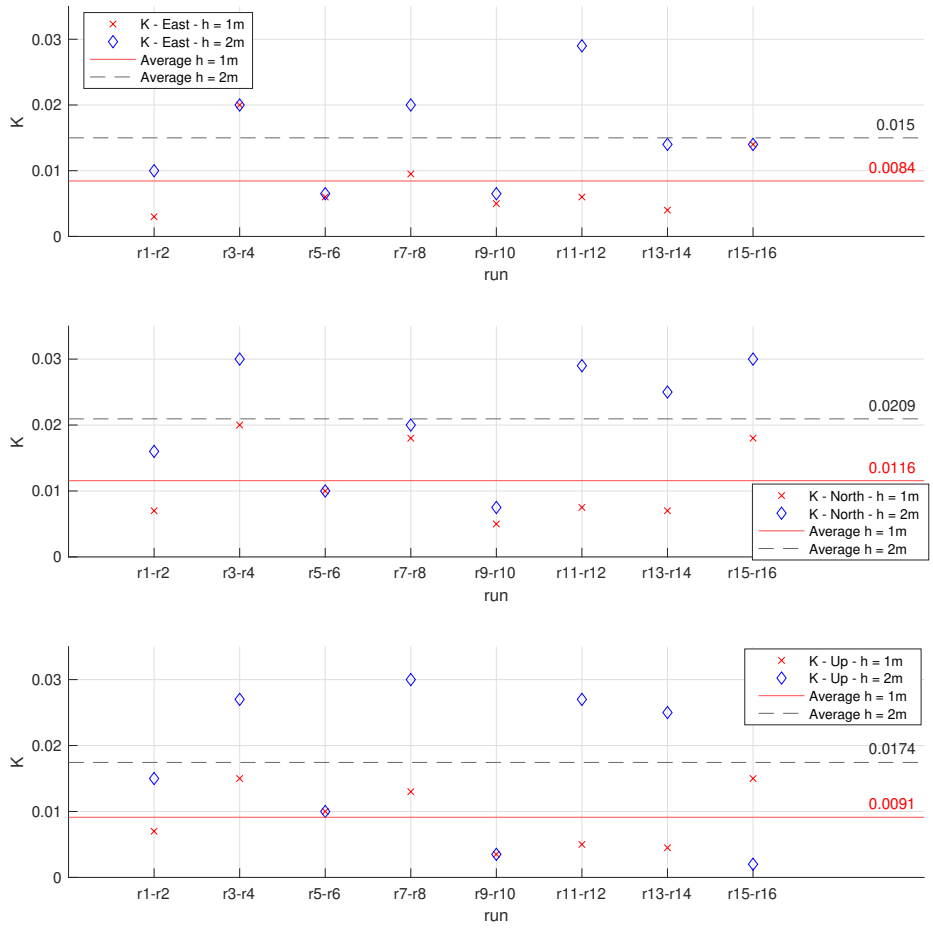

Figure 2.12: Comparison between RRW values for different heights.

Table 2.9: RRW coefficient K for different TAV

	h = 1m 100 lux YF: N		h = 2m 100 lux YF: N		h = 1m 100 lux YF: Y		h = 2m 100 lux YF: Y		h = 1m 250 lux YF: N		h = 2m 250 lux YF: N		h = 1m 250 lux YF: Y		h = 2m 250 lux YF: Y	
TAV [rad/s]	0.2	0.6	0.2	0.6	0.2	0.6	0.2	0.6	0.2	0.6	0.2	0.6	0.2	0.6	0.2	0.6
Run	1	3	2	4	5	7	6	8	9	11	10	12	13	15	14	16
K - East	0,003	0,02	0,01	0,02	0,006	0,0095	0,0065	0,02	0,005	0,006	0,0065	0,029	0,004	0,014	0,014	0,014
K - North	0,007	0,02	0,016	0,03	0,01	0,018	0,01	0,02	0,005	0,0075	0,0075	0,029	0,007	0,018	0,025	0,03
K - Up	0,007	0,015	0,015	0,027	0,01	0,013	0,01	0,01	0,0035	0,005	0,0035	0,027	0,0045	0,015	0,025	0,02

RRW - Comparison between different choices of TAV

The comparison between RRW values for different choices of TAV is shown in Table 2.9 and in Figure 2.13.

On average, the RRW coefficient K seems to increase when the TAV increases. In some runs such increment is lower, and this does not appear to be related to other factors.

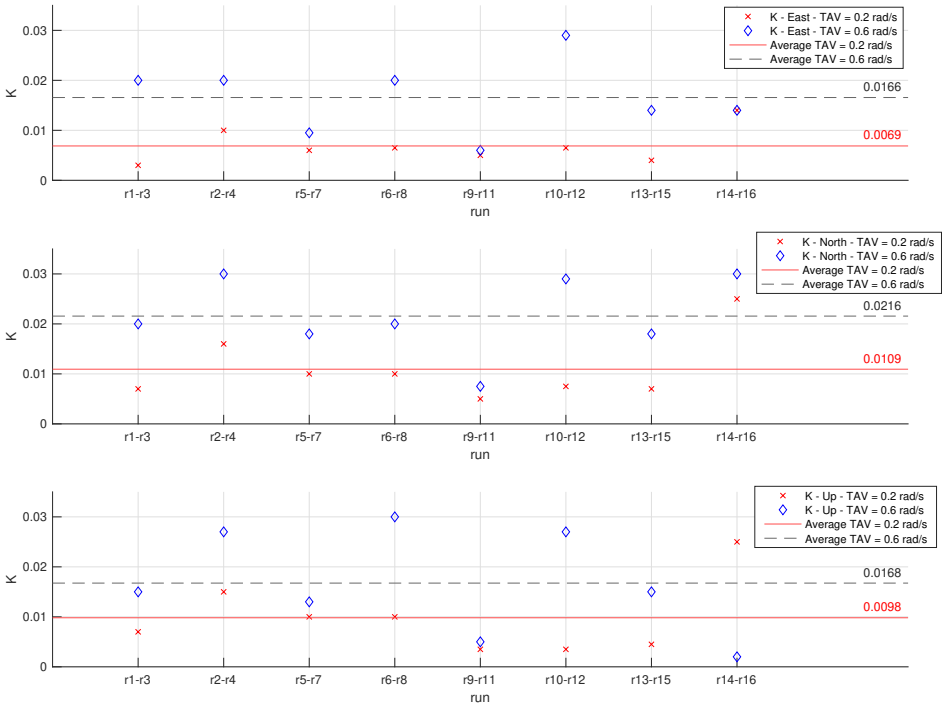

Figure 2.13: Comparison between RRW values for different TAV.

Table 2.10: RRW coefficient K with YF inactive or active

	h = 1m TAV* = 0.2 100 lux		h = 2m TAV = 0.2 100 lux		h = 1m TAV = 0.6 100 lux		h = 2m TAV = 0.6 100 lux		h = 1m TAV = 0.2 250 lux		h = 2m TAV = 0.2 250 lux		h = 1m TAV = 0.6 250 lux		h = 2m TAV = 0.6 250 lux	
YF:	N	Y	N	Y	N	Y	N	Y	N	Y	N	Y	N	Y	N	Y
Run	1	5	2	6	3	7	4	8	9	13	10	14	11	15	12	16
K - East	0,003	0,006	0,01	0,0065	0,02	0,0095	0,02	0,02	0,005	0,004	0,0065	0,014	0,006	0,014	0,029	0,014
K - North	0,007	0,01	0,016	0,01	0,02	0,018	0,03	0,02	0,005	0,007	0,0075	0,025	0,0075	0,018	0,029	0,03
K - Up	0,007	0,01	0,015	0,01	0,015	0,013	0,027	0,01	0,0035	0,0045	0,0035	0,025	0,005	0,015	0,027	0,02

***TAV is in [rad/s]**

RRW - Comparison between runs performed with and without the Yaw Following mode

The comparison between RRW values for the Yaw Following mode inactive or active is shown in Table 2.10 and in Figure 2.14.

It is not clear how the Yaw Following mode modifies the RRW coefficients. The trends are similar between the axes, but for each couple of runs the values oscillates without defining a pattern, and the averages of the coefficients with and without the Yaw Following mode are very similar.

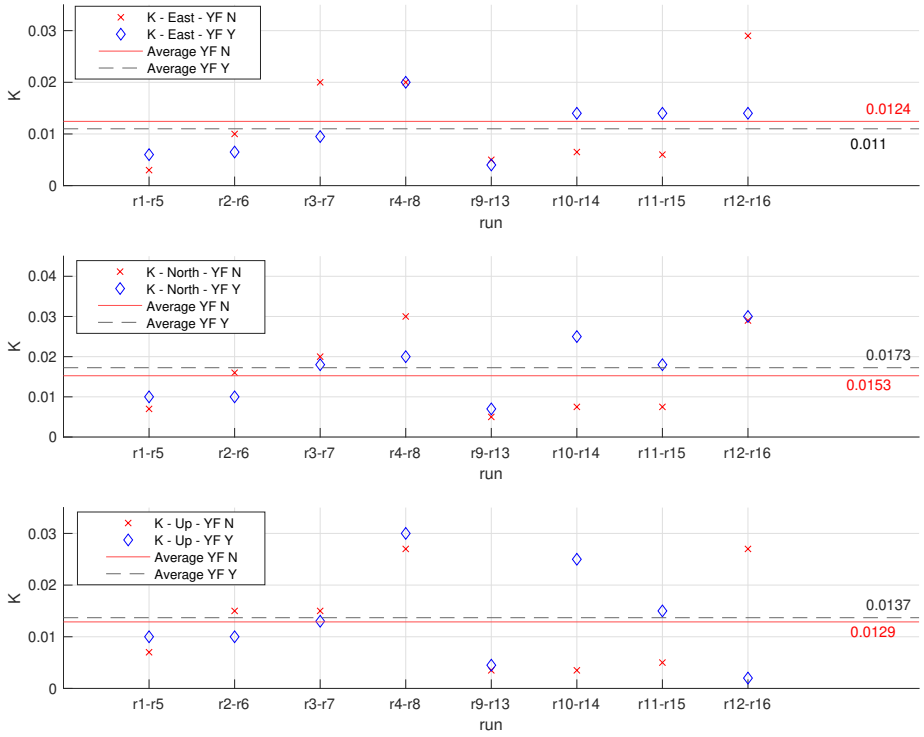

Figure 2.14: Comparison between RRW values with YF active or inactive.

Table 2.11: RRW coefficient K for different light intensities

	h = 1m TAV* = 0.2 YF: N		h = 2m TAV = 0.2 YF: N		h = 1m TAV = 0.6 YF: N		h = 2m TAV = 0.6 YF: N		h = 1m TAV = 0.2 YF: Y		h = 2m TAV = 0.2 YF: Y		h = 1m TAV = 0.6 YF: Y		h = 2m TAV = 0.6 YF: Y	
Light [lux]	**100**	**250**	**100**	**250**	**100**	**250**	**100**	**250**	**100**	**250**	**100**	**250**	**100**	**250**	**100**	**250**
Run	1	9	2	10	3	11	4	12	5	13	6	14	7	15	8	16
K - East	0,003	0,005	0,01	0,0065	0,02	0,006	0,02	0,029	0,006	0,004	0,0065	0,014	0,0095	0,014	0,02	0,014
K - North	0,007	0,005	0,016	0,0075	0,02	0,0075	0,03	0,029	0,01	0,007	0,01	0,025	0,018	0,018	0,02	0,03
K - Up	0,007	0,0035	0,015	0,0035	0,015	0,005	0,027	0,027	0,01	0,0045	0,01	0,025	0,013	0,015	0,01	0,02

***TAV is in [rad/s]**

RRW - Comparison between different choices of environment light intensities

The comparison between RRW values for different intensities of environmental light is shown in Table 2.11 and in Figure 2.15.

The values of RRW for axes East and North appears to be independent of the environmental light: the coefficient K oscillates from run to run, and no relation to other factors can be defined.

The RRW affecting the Up axis appears to increase when the light increases, but, by comparing this behaviour to the ones of the other axes, one can't exclude this could be just a random variation.

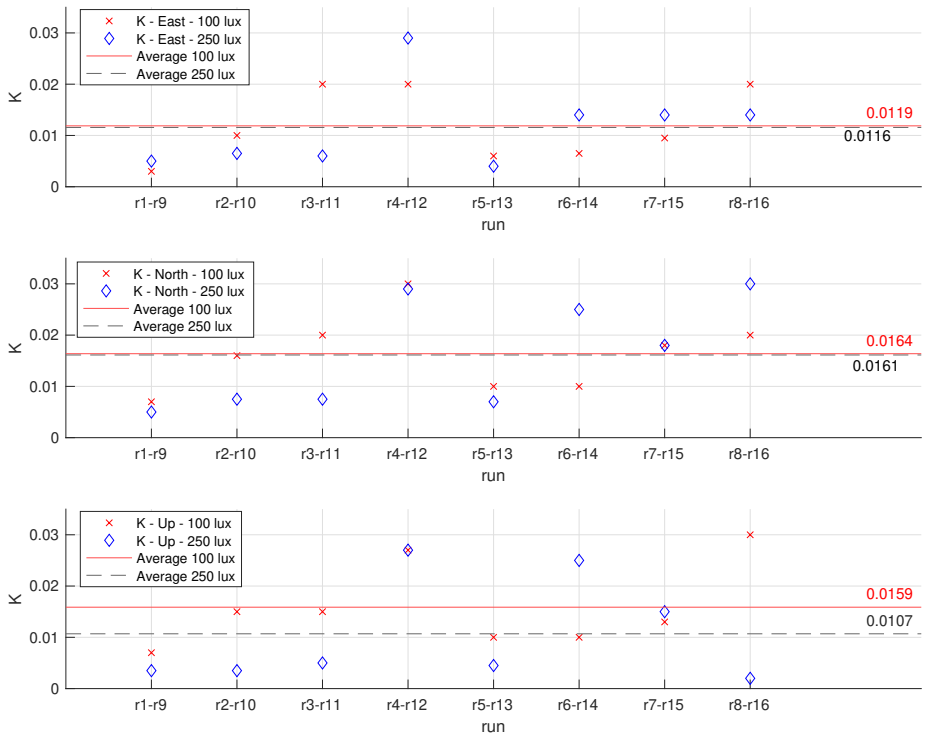

Figure 2.15: Comparison between RRW values for different environment light intensities.

Table 2.12: Gauss-Markov coefficient T_B for the different experiments

Run	1	2	3	4	5	6	7	8	9	10	11	12	13	14	15	16
Height [m]	1	2	1	2	1	2	1	2	1	2	1	2	1	2	1	2
TAV [rad/s]	0.2	0.2	0.6	0.6	0.2	0.2	0.6	0.6	0.2	0.2	0.6	0.6	0.2	0.2	0.6	0.6
YF	N	N	N	N	Y	Y	Y	Y	N	N	N	N	Y	Y	Y	Y
Light [lux]	100	100	100	100	100	100	100	100	250	250	250	250	250	250	250	250
T_B - East	10	10	10	10	10	10	10	0,1	0,1	0,1	0,1	0,1	0,1	0,1	0,1	0,1
T_B - North	10	10	10	10	10	1	0,1	0,1	0,1	0,1	0,1	0,1	0,1	0,1	0,1	0,1
T_B - Up	0,1	0,1	1	1	1	0,1	0,1	0,1	0,1	0,1	0,1	0,1	0,1	0,1	0,1	0,1

2.4.3 Gauss-Markov Process - Coefficient T_B

Comparison between axes East-North-Up

In Table 2.12 the values of the coefficient T_B are reported for each experiment. They are compared in Figure 2.16.

Due to the uncertainty on the dummy ADEV, the values of T_B have been estimated as powers of ten in order to perform the analysis by comparing their orders of magnitude. Their values oscillate between 0.1 and 10.

The variances of the values for each axis are:

- East: 25.7
- North: 22.1
- Up: 0.13

When the ambient light is 100 lux, T_B values of East and North axes are, on average, larger than the ones of Up axis.

When the light is set to 250 lux, T_B remains constant at 0.1 for all the axes.

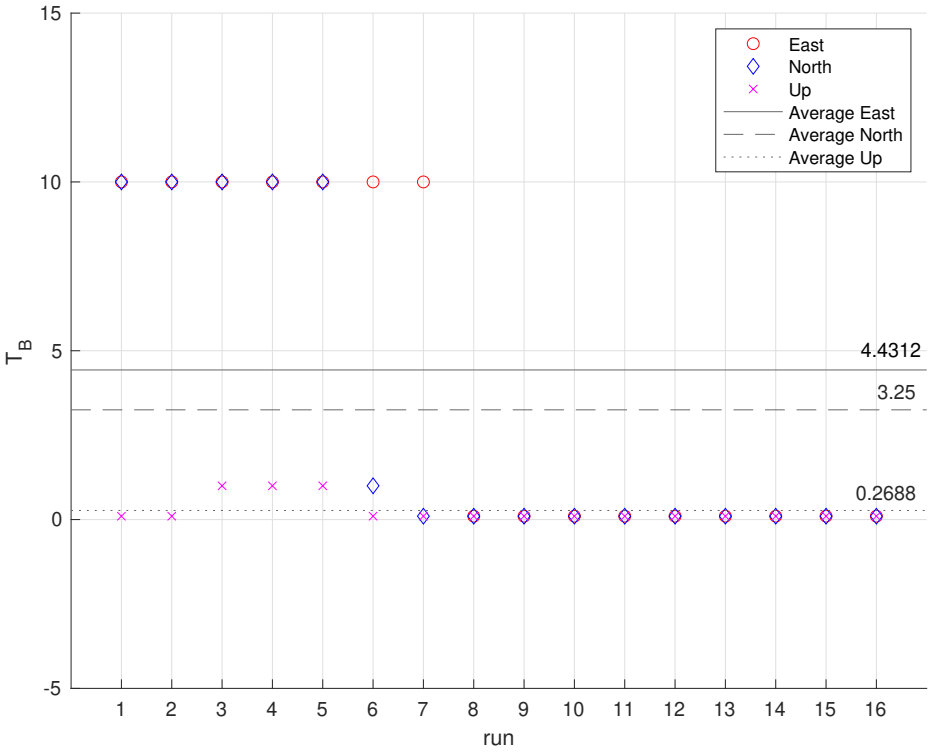

Figure 2.16: Comparison between T_B coefficients of axes East, North, Up for the different experiments.

Table 2.13: Gauss-Markov coefficient T_B for different heights

	TAV* = 0.2 YF: N 100 lux		TAV = 0.6 YF: N 100 lux		TAV = 0.2 YF: Y 100 lux		TAV = 0.6 YF: Y 100 lux		TAV = 0.2 YF: N 250 lux		TAV = 0.6 YF: N 250 lux		TAV = 0.2 YF: Y 250 lux		TAV = 0.6 YF: Y 250 lux	
Height:	1m | 2m		1m | 2m		1m | 2m		1m | 2m		1m | 2m		1m | 2m		1m | 2m		1m | 2m	
Run	1	2	3	4	5	6	7	8	9	10	11	12	13	14	15	16
T_B - East	10	10	10	10	10	10	10	0,1	0,1	0,1	0,1	0,1	0,1	0,1	0,1	0,1
T_B - North	10	10	10	10	10	1	0,1	0,1	0,1	0,1	0,1	0,1	0,1	0,1	0,1	0,1
T_B - Up	0,1	0,1	1	1	1	0,1	0,1	0,1	0,1	0,1	0,1	0,1	0,1	0,1	0,1	0,1

*TAV is in [rad/s]

T_B - Comparison between different choices of heights

The comparison between T_B values for different choices of heights is shown in Table 2.13 and in Figure 2.17.

The coefficient T_B appears to be independent of the height. In almost all the runs, T_B remains constant when the height is set from 1m to 2m.

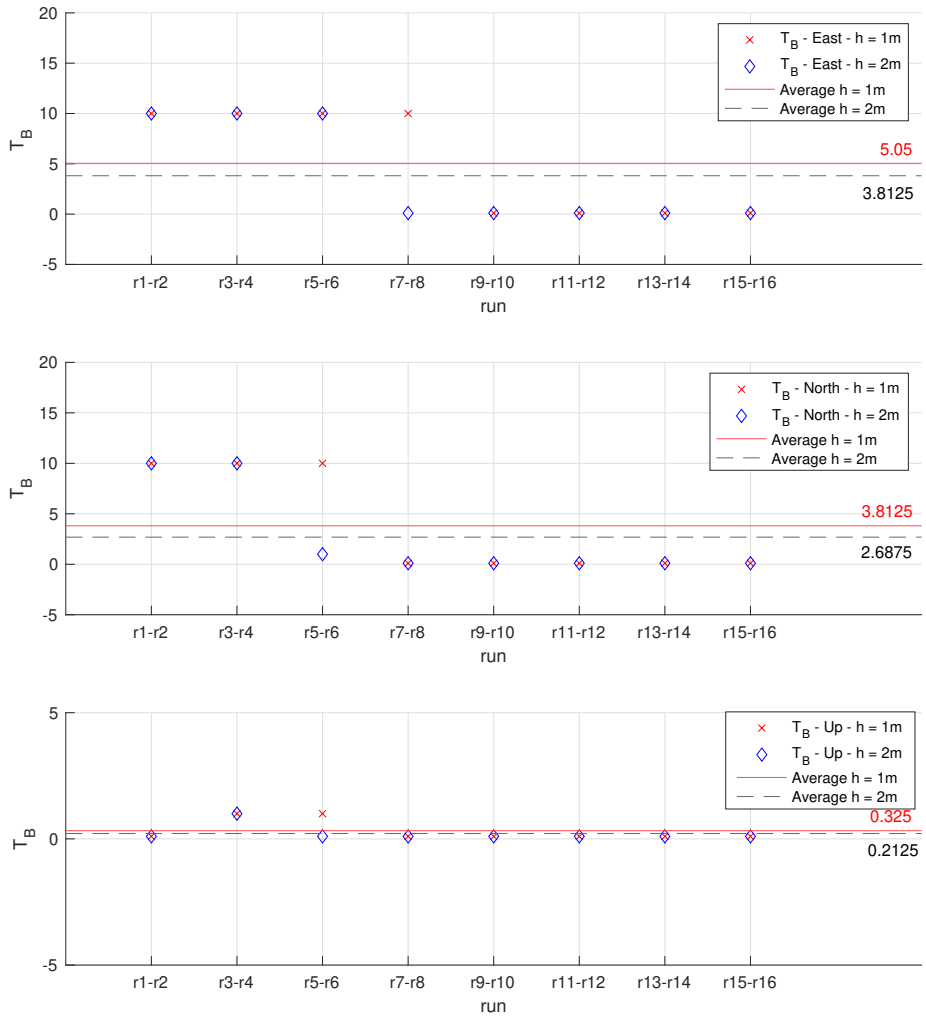

Figure 2.17: Comparison between T_B values for different heights.

Table 2.14: Gauss-Markov coefficient T_B for different TAV.

	h = 1m 100 lux YF: N		h = 2m 100 lux YF: N		h = 1m 100 lux YF: Y		h = 2m 100 lux YF: Y		h = 1m 250 lux YF: N		h = 2m 250 lux YF: N		h = 1m 250 lux YF: Y		h = 2m 250 lux YF: Y	
TAV [rad/s]	0.2	0.6	0.2	0.6	0.2	0.6	0.2	0.6	0.2	0.6	0.2	0.6	0.2	0.6	0.2	0.6
Run	1	3	2	4	5	7	6	8	9	11	10	12	13	15	14	16
T_B - East	10	10	10	10	10	10	10	0,1	0,1	0,1	0,1	0,1	0,1	0,1	0,1	0,1
T_B - North	10	10	10	10	10	0,1	1	0,1	0,1	0,1	0,1	0,1	0,1	0,1	0,1	0,1
T_B - Up	0,1	1	0,1	1	1	0,1	0,1	0,1	0,1	0,1	0,1	0,1	0,1	0,1	0,1	0,1

T_B - Comparison between different choices of TAV

The comparison between T_B values for different choices of TAV is shown in Table 2.14 and in Figure 2.18.

As for the height, the coefficient T_B appears to be independent of the TAV.

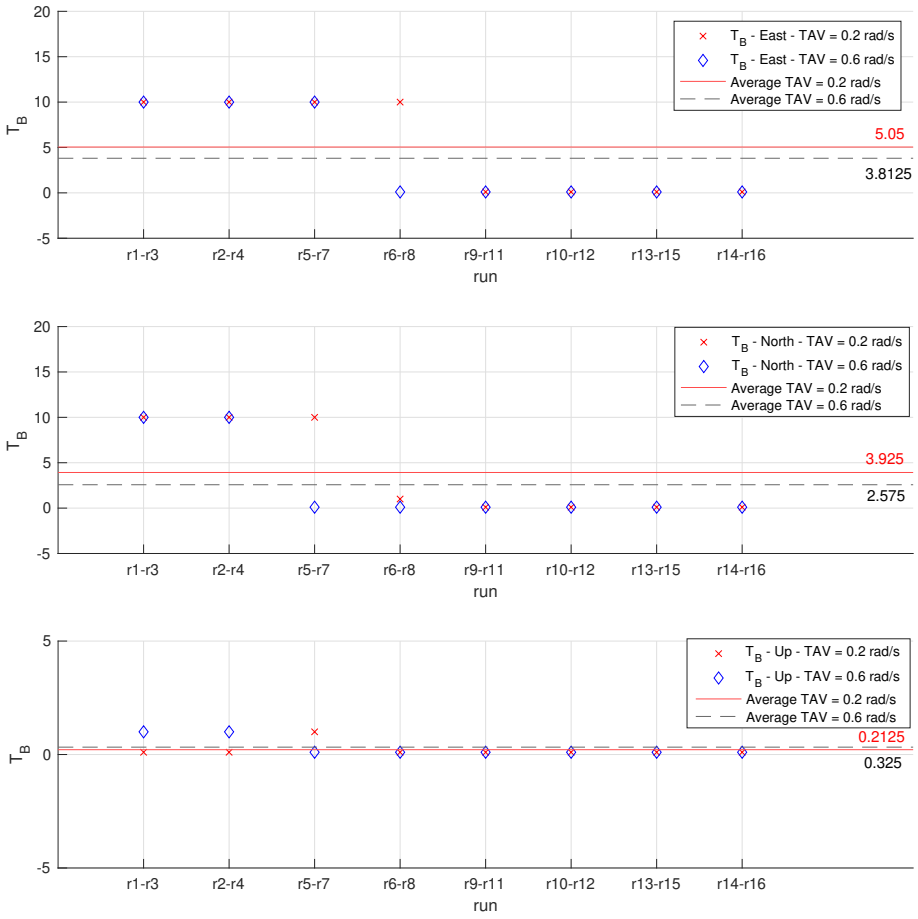

Figure 2.18: Comparison between T_B values for different TAV.

Table 2.15: Gauss-Markov coefficient T_B with YF inactive or active

	h = 1m TAV* = 0.2 100 lux		h = 2m TAV = 0.2 100 lux		h = 1m TAV = 0.6 100 lux		h = 2m TAV = 0.6 100 lux		h = 1m TAV = 0.2 250 lux		h = 2m TAV = 0.2 250 lux		h = 1m TAV = 0.6 250 lux		h = 2m TAV = 0.6 250 lux	
YF:	N	Y	N	Y	N	Y	N	Y	N	Y	N	Y	N	Y	N	Y
Run	1	5	2	6	3	7	4	8	9	13	10	14	11	15	12	16
T_B - East	10	10	10	10	10	10	10	0,1	0,1	0,1	0,1	0,1	0,1	0,1	0,1	0,1
T_B - North	10	10	10	1	10	0,1	10	0,1	0,1	0,1	0,1	0,1	0,1	0,1	0,1	0,1
T_B - Up	0,1	1	0,1	0,1	1	0,1	1	0,1	0,1	0,1	0,1	0,1	0,1	0,1	0,1	0,1

***TAV is in [rad/s]**

T_B - Comparison between runs performed with and without the Yaw Following mode

The comparison between T_B values for the Yaw Following mode inactive or active is shown in Table 2.15 and in Figure 2.19.

The coefficient T_B for axes East and Up appears to be independent of the activation of the Yaw Following mode.

For the North axis, the activation of the Yaw Following in case of low environmental light is associated with a decrease of T_B, in three couples of run out of four.

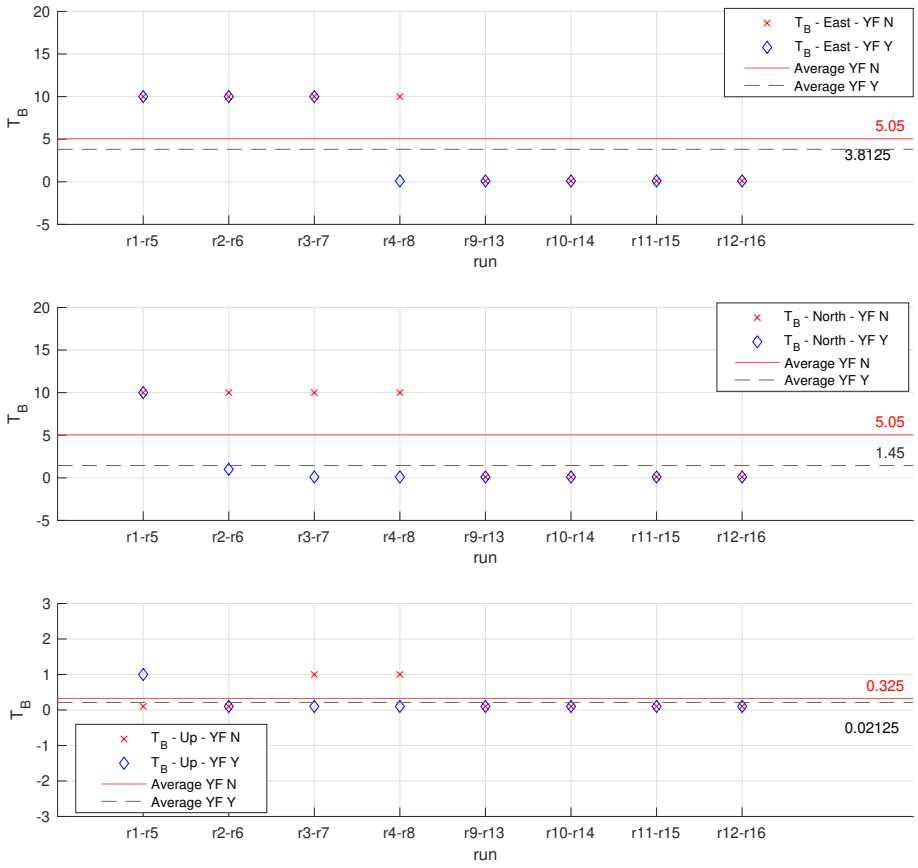

Figure 2.19: Comparison between T_B values with YF active or inactive.

Table 2.16: Gauss-Markov coefficient T_B for different light intensities.

	h = 1m TAV* = 0.2 YF: N		h = 2m TAV = 0.2 YF: N		h = 1m TAV = 0.6 YF: N		h = 2m TAV = 0.6 YF: N		h = 1m TAV = 0.2 YF: Y		h = 2m TAV = 0.2 YF: Y		h = 1m TAV = 0.6 YF: Y		h = 2m TAV = 0.6 YF: Y	
Light [lux]	100 | 250		100 | 250		100 | 250		100 | 250		100 | 250		100 | 250		100 | 250		100 | 250	
Run	1	9	2	10	3	11	4	12	5	13	6	14	7	15	8	16
T_B - East	10	0,1	10	0,1	10	0,1	10	0,1	10	0,1	10	0,1	10	0,1	0,1	0,1
T_B - North	10	0,1	10	0,1	10	0,1	10	0,1	10	0,1	1	0,1	0,1	0,1	0,1	0,1
T_B - Up	0,1	0,1	0,1	0,1	1	0,1	1	0,1	1	0,1	0,1	0,1	0,1	0,1	0,1	0,1

*TAV is in [rad/s]

T_B - Comparison between different choices of environment light intensities

The comparison between T_B values for different intensities of environmental light is shown in Table 2.16 and in Figure 2.20.

The coefficient T_B appears to be related to the environmental light, for axes East and North.

For East axis, seven couples out of eight present an increase of T_B when the ambient light is set from 100 lux to 250 lux.

For North axis, this increase is present when the Yaw Following is inactive, while, when it is active, T_B is small even with low light.

For Up axis, the increase is present only in few runs, while in the others T_B remains constant.

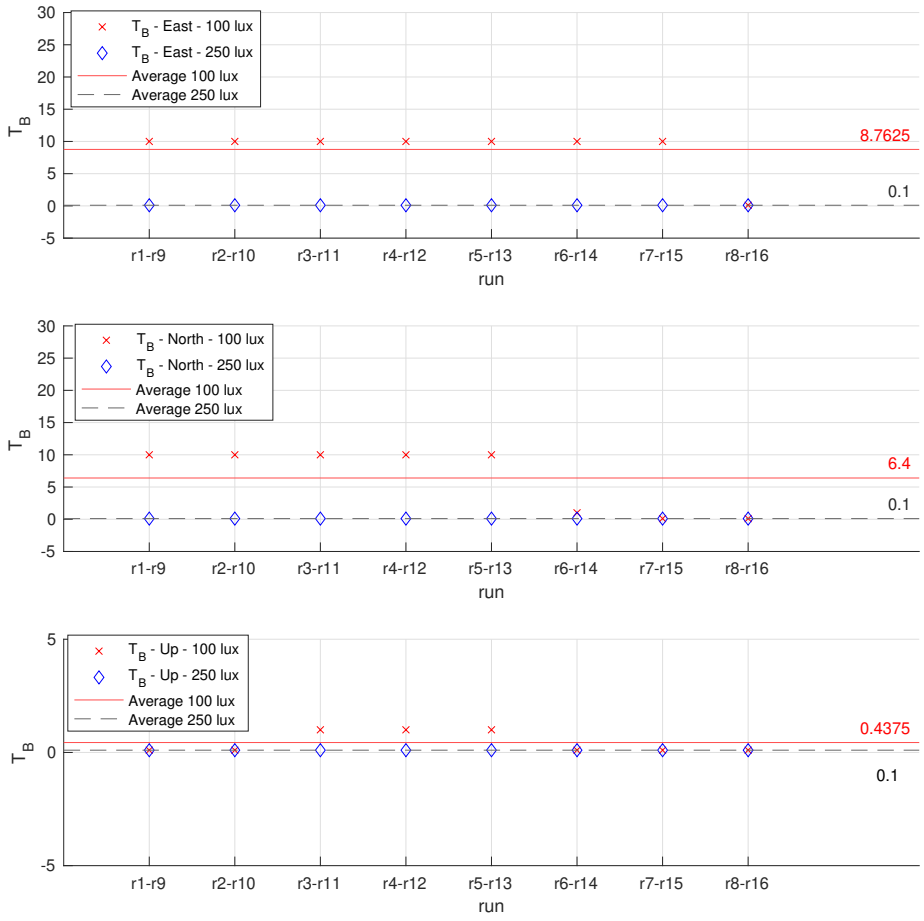

Figure 2.20: Comparison between T_B values for different environment light intensities.

Table 2.17: Gauss-Markov coefficient Q_B for the different experiments.

Run	1	2	3	4	5	6	7	8	9	10	11	12	13	14	15	16
Quota [m]	1	2	1	2	1	2	1	2	1	2	1	2	1	2	1	2
TAV [rad/s]	0.2	0.2	0.6	0.6	0.2	0.2	0.6	0.6	0.2	0.2	0.6	0.6	0.2	0.2	0.6	0.6
YF	N	N	N	N	Y	Y	Y	Y	N	N	N	N	Y	Y	Y	Y
Light [lux]	100	100	100	100	100	100	100	100	250	250	250	250	250	250	250	250
Q_B - East	1E-05	1E-06	1E-05	7E-05	1E-06	1E-06	1E-06	1E-06	1E-07	1E-07	1E-07	1E-07	1E-07	1E-06	1E-06	1E-06
Q_B - North	1E-05	1E-06	1E-05	1E-05	1E-06	1E-06	1E-06	1E-06	1E-07	1E-07	1E-07	1E-07	1E-07	1E-06	1E-06	1E-06
Q_B - Up	1E-05	1E-05	5E-05	2E-05	1E-06	1E-07	1E-07	1E-07	1E-07	1E-07	1E-06	1E-06	1E-06	1E-06	1E-07	1E-07

2.4.4 Gauss-Markov Process - Coefficient Q_B

Comparison between axes East-North-Up

In Table 2.17 the values of the coefficient Q_B are reported for each experiment. They are compared in Figure 2.21, in logarithmic scale.

East and Up axes have very similar average values, while North axis has a lower mean.

The variances of the values for each axis are:

- East: 3.0011e-10
- North: 1.4361e-11
- Up: 1.6884e-10

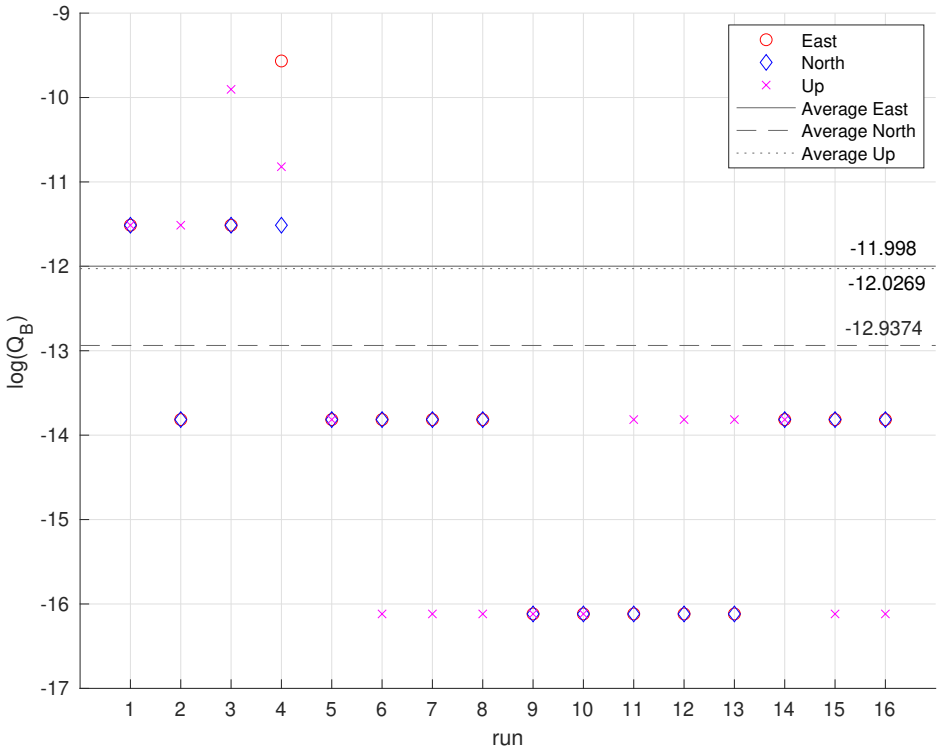

Figure 2.21: Comparison between Q_B coefficients of axes East, North, Up for the different experiments, in log scale.

Table 2.18: Gauss-Markov coefficient Q_B for different heights.

	TAV* = 0.2 YF: N 100 lux		TAV = 0.6 YF: N 100 lux		TAV = 0.2 YF: Y 100 lux		TAV = 0.6 YF: Y 100 lux		TAV = 0.2 YF: N 250 lux		TAV = 0.6 YF: N 250 lux		TAV = 0.2 YF: Y 250 lux		TAV = 0.6 YF: Y 250 lux	
Height:	**1m**	**2m**	**1m**	**2m**	**1m**	**2m**	**1m**	**2m**	**1m**	**2m**	**1m**	**2m**	**1m**	**2m**	**1m**	**2m**
Run	1	2	3	4	5	6	7	8	9	10	11	12	13	14	16	15
Q_B - East	1E-05	1E-06	1E-05	7E-05	1E-06	1E-06	1E-06	1E-06	1E-07	1E-07	1E-07	1E-07	1E-07	1E-06	1E-06	1E-06
Q_B - North	1E-05	1E-06	1E-05	1E-05	1E-06	1E-06	1E-06	1E-06	1E-07	1E-07	1E-07	1E-07	1E-07	1E-06	1E-06	1E-06
Q_B - Up	1E-05	1E-05	5E-05	2E-05	1E-06	1E-07	1E-07	1E-07	1E-07	1E-07	1E-06	1E-06	1E-06	1E-06	1E-07	1E-07

***TAV is in [rad/s]**

Q_B - Comparison between different choices of heights

The comparison between Q_B values for different choices of heights is shown in Table 2.18 and in Figure 2.22, in logarithmic scale.

The coefficient Q_B appears to be independent of the height. In most of the runs, the change from 1m to 2m is not associated with a change of Q_B. In some runs there are variations (which change from axis to axis), but they do not seem to be associated with other factors.

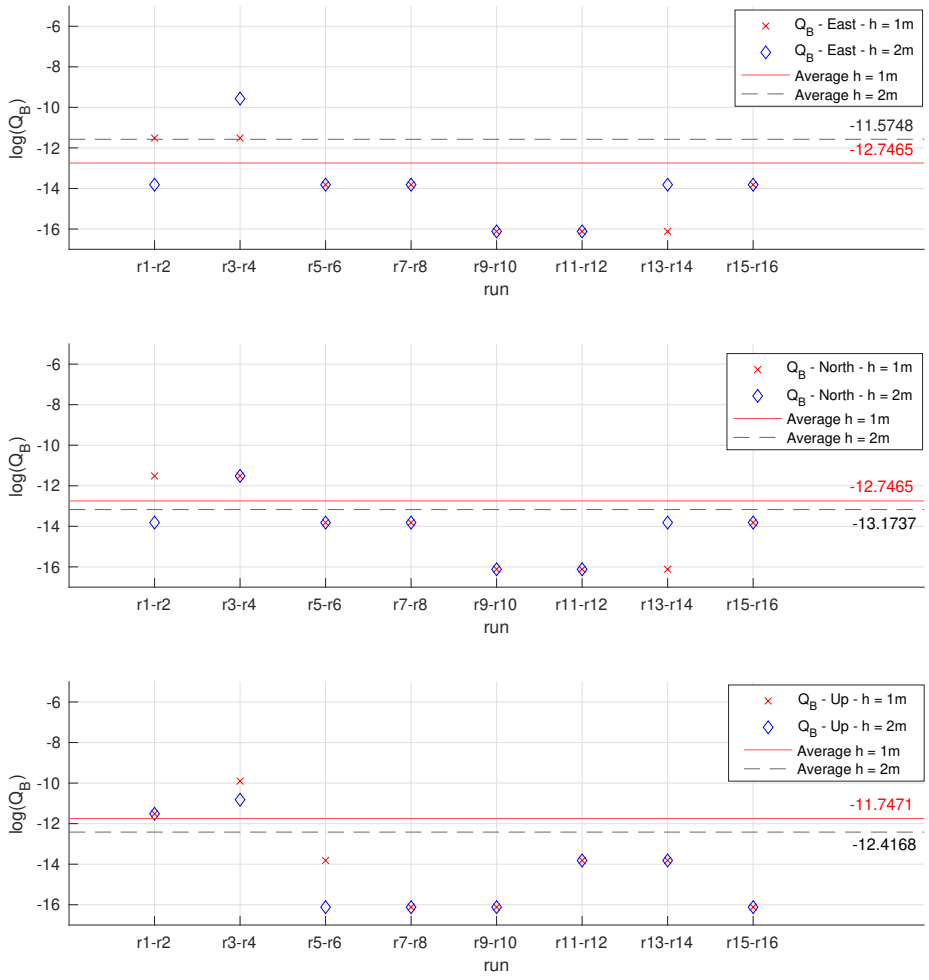

Figure 2.22: Comparison between Q_B values for different heights, in log scale.

Table 2.19: Gauss-Markov coefficient Q_B for different TAV

	h = 1m 100 lux YF: N		h = 2m 100 lux YF: N		h = 1m 100 lux YF: Y		h = 2m 100 lux YF: Y		h = 1m 250 lux YF: N		h = 2m 250 lux YF: N		h = 1m 250 lux YF: Y		h = 2m 250 lux YF: Y	
TAV [rad/s]	0.2	0.6	0.2	0.6	0.2	0.6	0.2	0.6	0.2	0.6	0.2	0.6	0.2	0.6	0.2	0.6
Run	1	3	2	4	5	7	6	8	9	11	10	12	13	15	14	16
Q_B - East	1E-05	1E-05	1E-06	7E-05	1E-06	1E-06	1E-06	1E-06	1E-07	1E-07	1E-07	1E-07	1E-07	1E-06	1E-06	1E-06
Q_B - North	1E-05	1E-05	1E-06	1E-05	1E-06	1E-06	1E-06	1E-06	1E-07	1E-07	1E-07	1E-07	1E-07	1E-06	1E-06	1E-06
Q_B - Up	1E-05	5E-05	1E-05	2E-05	1E-06	1E-07	1E-07	1E-07	1E-07	1E-06	1E-07	1E-06	1E-06	1E-07	1E-06	1E-07

Q_B - Comparison between different choices of TAV

The comparison between Q_B values for different choices of TAV is shown in Table 2.19 and in Figure 2.23, in logarithmic scale.

The coefficient Q_B appears to be independent of the TAV, for axes East and North: when the TAV increases the only couples of runs which present a change are r2-r4 and r13-r15, but these couples don't have characteristics in common.

Axis Up shows a different behaviour: it appears that when the Yaw Following is inactive (run 1-3, 2-4, 9-11, 10-12) an increase in TAV is associated with a rise of Q_B. When the Yaw Following is active and the TAV increases, Q_B decreases (except for runs 6-8, where Q_B is contant).

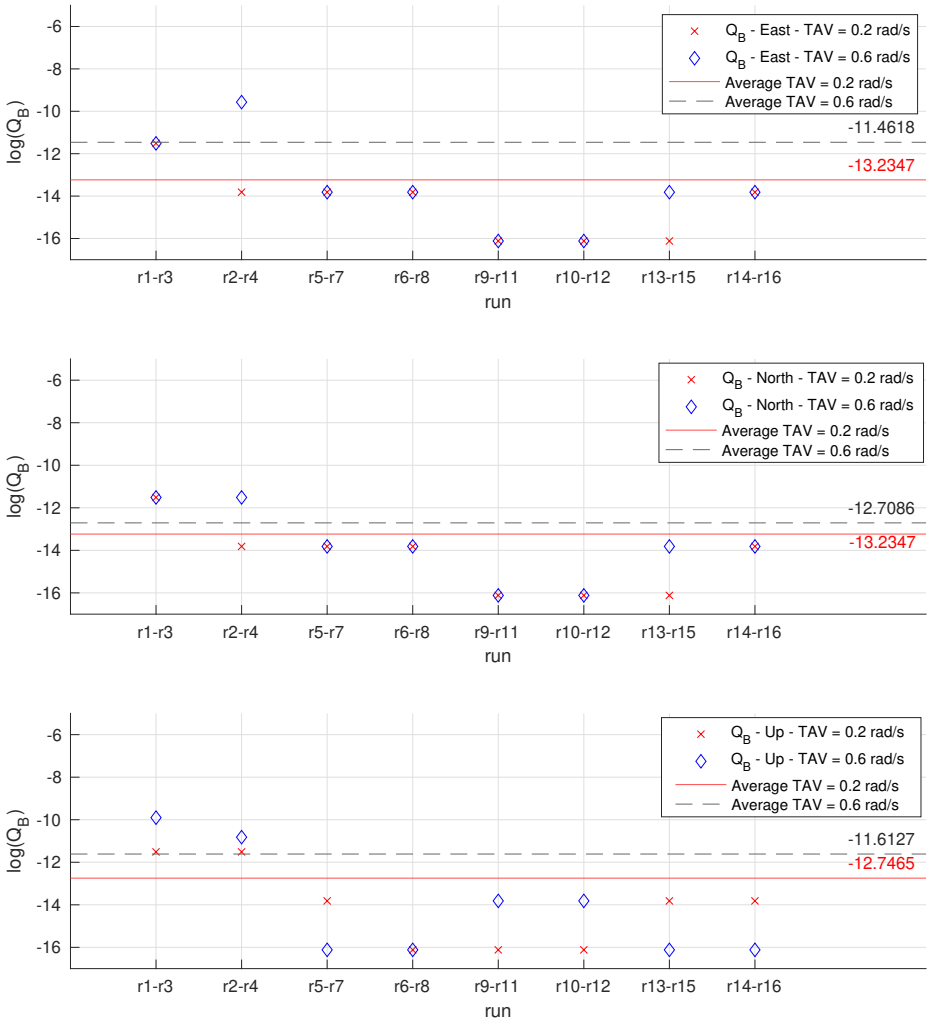

Figure 2.23: Comparison between Q_B values for different TAV, in log scale.

Table 2.20: Gauss-Markov coefficient Q_B with YF inactive or active.

	h = 1m TAV* = 0.2 100 lux		h = 2m TAV = 0.2 100 lux		h = 1m TAV = 0.6 100 lux		h = 2m TAV = 0.6 100 lux		h = 1m TAV = 0.2 250 lux		h = 2m TAV = 0.2 250 lux		h = 1m TAV = 0.6 250 lux		h = 2m TAV = 0.6 250 lux	
YF:	N	Y	N	Y	N	Y	N	Y	N	Y	N	Y	N	Y	N	Y
Run	1	5	2	6	3	7	4	8	9	13	10	14	11	15	12	16
Q_B - East	1E-05	1E-06	1E-06	1E-06	1E-05	1E-06	7E-05	1E-06	1E-07	1E-07	1E-07	1E-06	1E-07	1E-06	1E-07	1E-06
Q_B - North	1E-05	1E-06	1E-06	1E-06	1E-05	1E-06	1E-05	1E-06	1E-07	1E-07	1E-07	1E-06	1E-07	1E-06	1E-07	1E-06
Q_B - Up	1E-05	1E-06	1E-05	1E-07	5E-05	1E-07	2E-05	1E-07	1E-07	1E-06	1E-07	1E-06	1E-06	1E-07	1E-06	1E-07

***TAV is in [rad/s]**

Q_B - Comparison between runs performed with and without the Yaw Following mode

The comparison between Q_B values for the Yaw Following mode inactive or active is shown in Table 2.20 and in Figure 2.24, in logarithmic scale.

For axes East and North, the effect of the Yaw Following on the coefficient Q_B appears to be depending on the ambient light. When the light measured is 100 lux , the activation of the Yaw Following is associated with a decrease of Q_B (except for runs 2-6). When the light measured is 250 lux, the activation of the Yaw Following is associated with an increase of Q_B (except for runs 9-13).

For axis Up, on average the activation of the Yaw Following is related to a decrease of Q_B, except for runs 9-13 and 10-14, both characterized by stronger ambient light and low TAV.

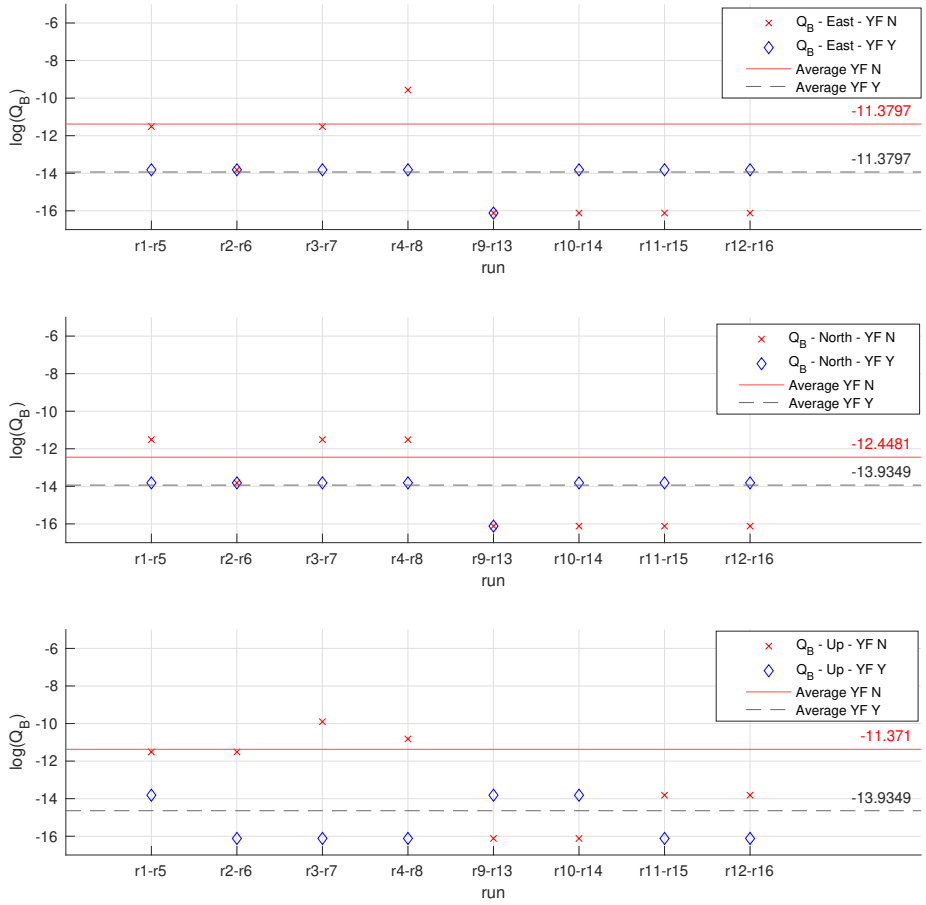

Figure 2.24: Comparison between Q_B values with YF active or inactive, in log scale.

Table 2.21: Gauss-Markov coefficient Q_B for different light intensities.

	h = 1m TAV* = 0.2 YF: N		h = 2m TAV = 0.2 YF: N		h = 1m TAV = 0.6 YF: N		h = 2m TAV = 0.6 YF: N		h = 1m TAV = 0.2 YF: Y		h = 2m TAV = 0.2 YF: Y		h = 1m TAV = 0.6 YF: Y		h = 2m TAV = 0.6 YF: Y	
Light [lux]	100 | 250		100 | 250		100 | 250		100 | 250		100 | 250		100 | 250		100 | 250		100 | 250	
Run	1	9	2	10	3	11	4	12	5	13	6	14	7	15	8	16
Q_B - East	1E-05	1E-07	1E-06	1E-07	1E-05	1E-07	7E-05	1E-07	1E-06	1E-07	1E-06	1E-06	1E-06	1E-06	1E-06	1E-06
Q_B - North	1E-05	1E-07	1E-06	1E-07	1E-05	1E-07	1E-05	1E-07	1E-06	1E-07	1E-06	1E-06	1E-06	1E-06	1E-06	1E-06
Q_B - Up	1E-05	1E-07	1E-05	1E-07	5E-05	1E-06	2E-05	1E-06	1E-06	1E-06	1E-07	1E-06	1E-07	1E-07	1E-07	1E-07

*TAV is in [rad/s]

Q_B - Comparison between different choices of environment light intensities

The comparison between Q_B values for different intensities of environmental light is shown in Table 2.21 and in Figure 2.25, in logarithmic scale.

As shown in the previous paragraph, there seems to be a correlation between the coefficient Q_B, the Yaw Following and the ambient light.

The values of Q_B decrease if the Yaw Following is inactive and the ambient light is set from 100 lux to 250 lux. When the Yaw Following is active, Q_B is lower even with for 100 lux. Exceptions are the couples r5-r13 for both East and North, and couple r6-r14 Up.

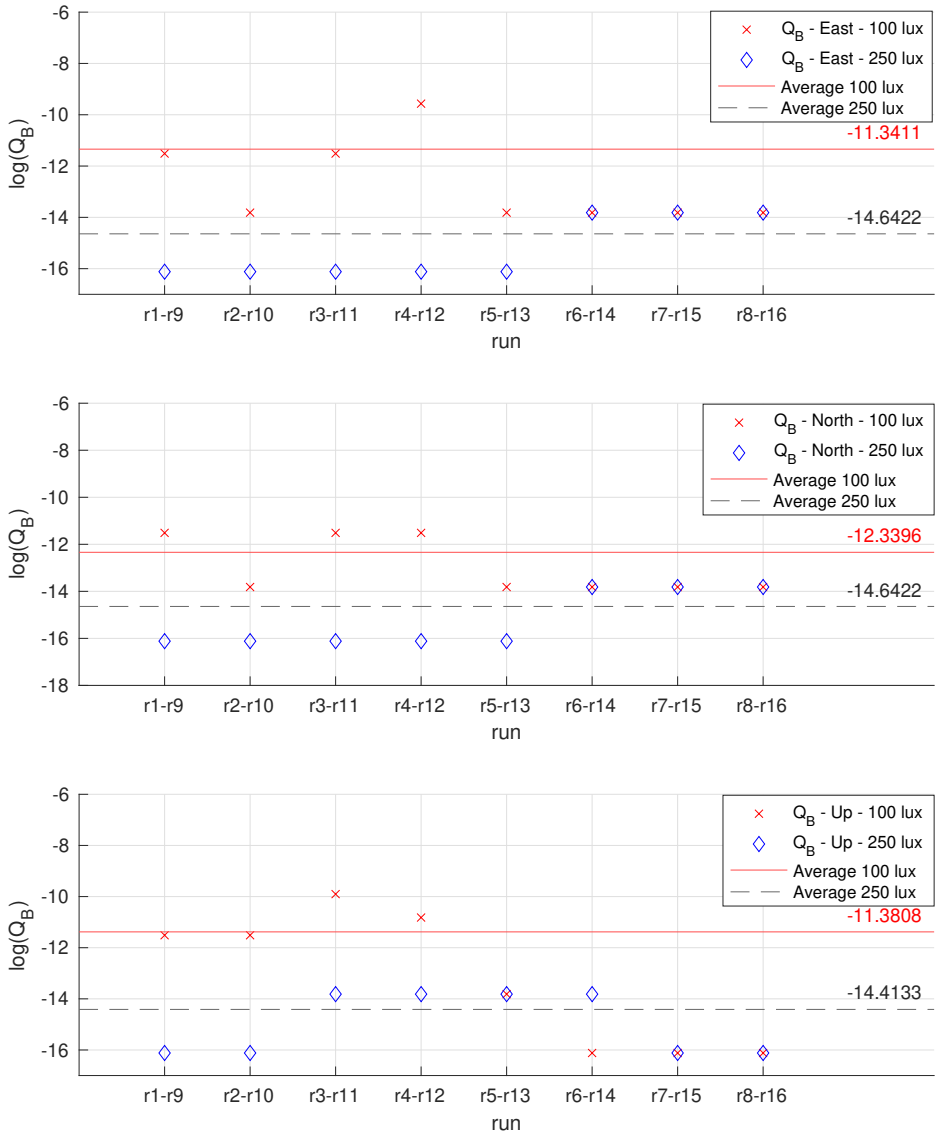

Figure 2.25: Comparison between Q_B values for different environment light intensities, in log scale.

2.5 Overview of the Results

As shown in Section 2.4, the AVAR analysis can give valuable information about the characteristics of the noise acting on the system, and how they vary when given parameters of the system change.

The major results obtained in terms of relation between noise coefficients and parameters of the experiments are summarized in the following list.

- ARW coefficient N: for axes East and North (not enough information is available for axis Up), the coefficient N appears to increase when the Yaw Following is activated. For all the axes, N appears to increase when the ambient light increases.

- RRW coefficient K: for all the axes, the coefficient K appears to increase if the height or the speed increase.

- GM coefficients T_B and Q_B: these coefficients appear to be related to the ambient light and the Yaw Following mode, even though each axis presents a different behaviour.

  In general, Q_B is lower when the ambient light is stronger, while the effects of the Yaw Following depend on the light itself and on the considered axis. Q_B for axis Up appears also to be influenced by the speed.

  The coefficient T_B most of the time increases when the ambient light is set to larger values. For axis North this behaviour appears to be influenced by the Yaw Following.

Even though a better approximation of the ADEV is required in order to obtain more accurate numerical values for each coefficient, the general trends and the relations with the mentioned parameters represent a useful achievement in the investigation of the noise dynamics affecting the visual odometry system. One can obtain more precise results by adding other noise types while constructing the dummy ADEV, and by extending the length of the observation time during the experiments.

2.6 Model discretization and Kalman predictor

In this section, a discrete time model is obtained from the continuous-time state state representation - equations (1.25), (1.26), (1.27) - and a Kalman predictor is constructed to compare the AVAR-based noise model with the experimental data. An example with real data is then provided.

2.6.1 Discretization of the state space representation

Since the visual odometry system works in discrete time, taking as input pictures with a certain frequency, its simulation requires a discrete-time description of its dynamics.

The discretization of the continuous-time state space representations consists in two steps: the first one is the discretization of the dynamic equation (1.25) and of the process noise matrix of equation (1.27), and the second one is the discretization of the output equation (1.26) and of the process noise PSD matrix of ω_N.

Discretization of the dynamics equation

The discretization process of this kind of linear time-continuous systems of differential equations is explained in [12].

Considering equation (1.25), it can be written as:

$$\begin{Bmatrix} \dot{z}_B \\ \dot{z_K} \end{Bmatrix} = A \begin{Bmatrix} z_B \\ z_K \end{Bmatrix} + B \begin{Bmatrix} \omega_B \\ \omega_K \end{Bmatrix} \tag{2.2}$$

where:

$$A = \begin{bmatrix} -\frac{1}{T_B} & 0 \\ 0 & 0 \end{bmatrix} \qquad B = \begin{bmatrix} 1 & 0 \\ 0 & 1 \end{bmatrix} \tag{2.3}$$

Its equivalent in discrete time is:

$$\begin{Bmatrix} z_{Bd}(t+1) \\ z_{Kd}(t+1) \end{Bmatrix} = A_d \begin{Bmatrix} z_{Bd}(t) \\ z_{Kd}(t) \end{Bmatrix} + B_d \begin{Bmatrix} \omega_{Bd}(t) \\ \omega_{Kd}(t) \end{Bmatrix} \tag{2.4}$$

where z_{Bd} and z_{Kd} are respectively the GM process noise and the RRW noise in discrete time, ω_{Bd} and ω_{Kd} are discrete-time white noises with PSD Q_d (yet to be introduced) and the matrix B_d is simply $B_d = B$. The matrix A_d is:

$$A_d = e^{AT_z} = \begin{bmatrix} e^{-\frac{T_z}{T_B}} & 0 \\ 0 & 1 \end{bmatrix} \tag{2.5}$$

where T_z is the sampling interval of the ZED camera.

The discrete-time process noise PSD matrix Q_d (equivalent of Q in discrete time) for Bias Instability and RRW is computed as follows:

$$Q_d = \int_0^{T_z} e^{(T_z-s)A} B Q B^T (e^{(T_z-s)A})^T \, ds \tag{2.6}$$

Substituting A,B and Q yields:

$$\begin{aligned} Q_d &= \int_0^{T_z} \exp\Big(\begin{bmatrix} -\frac{1}{T_B}(T_z - s) & 0 \\ 0 & 0 \end{bmatrix} \Big) \begin{bmatrix} 1 & 0 \\ 0 & 1 \end{bmatrix} \begin{bmatrix} Q_B & 0 \\ 0 & K^2 \end{bmatrix} \begin{bmatrix} 1 & 0 \\ 0 & 1 \end{bmatrix} * \\ &* \Big(\exp \begin{bmatrix} -\frac{1}{T_B}(T_z - s) & 0 \\ 0 & 0 \end{bmatrix} \Big)^T ds = \\ &= \int_0^{T_z} \begin{bmatrix} \exp(-\frac{1}{T_B}(T_z - s)) & 0 \\ 0 & 0 \end{bmatrix} \begin{bmatrix} 1 & 0 \\ 0 & 1 \end{bmatrix} \begin{bmatrix} Q_B & 0 \\ 0 & K^2 \end{bmatrix} \begin{bmatrix} 1 & 0 \\ 0 & 1 \end{bmatrix} * \\ &* \begin{bmatrix} \exp(-\frac{1}{T_B}(T_z - s)) & 0 \\ 0 & 0 \end{bmatrix}^T ds = \\ &= \begin{bmatrix} Q_B \int_0^{T_z} \exp(-2\frac{T_z - s}{T_B})\, ds & 0 \\ 0 & K^2 T_z \end{bmatrix} = \\ &= \begin{bmatrix} \frac{Q_B T_B}{2}(1 - \exp(-2\frac{T_z}{T_B})) & 0 \\ 0 & K^2 T_z \end{bmatrix} \end{aligned} \tag{2.7}$$

Discretization of the output equation

The discrete-time equivalent of equation (1.26) is derived in section V-B of [13]:

$$z_d(t+1) = \begin{bmatrix} 1 & 1 \end{bmatrix} \begin{Bmatrix} z_{Bd}(t) \\ z_{Kd}(t) \end{Bmatrix} + \omega_{Nd} \tag{2.8}$$

where z_d is the total discrete-time noise and ω_{Nd} is a discrete-time white noise with PSD Q_{Nd}:

$$Q_{Nd} = \frac{N^2}{T_z} \tag{2.9}$$

Discrete-time dynamic system

The discrete-time state space representation of the dynamics of the noise is therefore:

$$\begin{Bmatrix} z_{Bd}(t+1) \\ z_{Kd}(t+1) \end{Bmatrix} = A_d \begin{Bmatrix} z_{Bd}(t) \\ z_{Kd}(t) \end{Bmatrix} + B_d \begin{Bmatrix} \omega_{Bd}(t) \\ \omega_{Kd}(t) \end{Bmatrix} \tag{2.10}$$

$$z_d(t+1) = \begin{bmatrix} 1 & 1 \end{bmatrix} \begin{Bmatrix} z_{Bd}(t) \\ z_{Kd}(t) \end{Bmatrix} + \omega_{Nd}(t) \tag{2.11}$$

where ω_{Bd} and ω_{Kd} are white noises driven by the discrete-time PSD matrix Q_d and ω_{Nd} is a white noise driven by the discrete-time PSD matrix Q_{Nd}.

2.6.2 Kalman predictor

Once the state space system has been discretized, a Kalman predictor can be constructed in order to compare the noise ADEV-based model to the real noise dynamics.

Being the dynamic matrix A_d a simple 2x2 diagonal matrix, the Kalman predictor can be easily represented as shown in diagram of Figure 2.26.

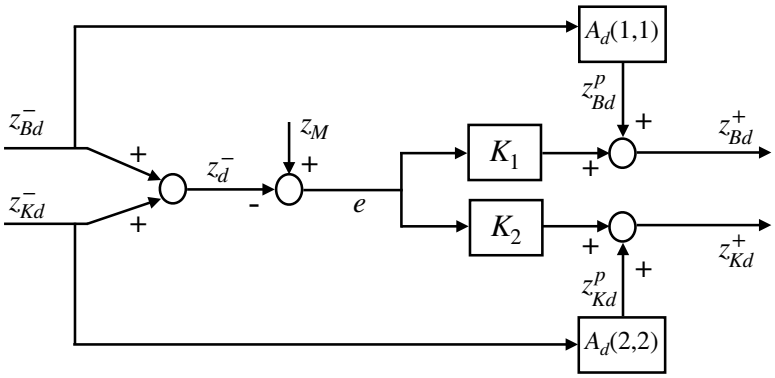

Figure 2.26: Kalman predictor diagram.

For each iteration, a prediction is formulated starting from the values of z_{Bd} and z_{Kd} of the previous iteration, namely z^-_{Bd} and z^-_{Kd}. The prediction simply consists in the values of the noises z^p_{Bd} and z^p_{Kd} obtained by the discrete time system - equation (2.10) and (2.11) - one step ahead in time:

$$z^p_{Bd} = z^-_{Bd} A_d(1,1) \qquad z^p_{Kd} = z^-_{Kd} A_d(2,2) \tag{2.12}$$

The error e is then computed between the total noise forecasted by the previous iteration $z^-_d = z^-_{Bd} + z^-_{Kd}$ and the real total noise z_M of the current iteration available from data:

$$e = z_M - z^-_d \tag{2.13}$$

The new forecasts of the Bias and RRW noises, namely z^+_{Bd} and z^+_{Kd}, are the result of the weighing between the predicted noises z^p_{Bd}, z^p_{Kd} and the information contained in the error. The update equations are:

$$z^+_{Bd} = z^p_{Bd} + \bar{K}_1 e \qquad z^+_{Kd} = z^p_{Kd} + \bar{K}_2 e \tag{2.14}$$

where the Kalman gains $\bar{K}_1$ and $\bar{K}_2$ are obtained by computing:

$$\bar{K} = \begin{bmatrix} \bar{K}_1 \\ \bar{K}_2 \end{bmatrix} = \left(C_d P C_d^T + Q_{Nd}\right)^{-1} \left(C_d P A_d^T\right) \tag{2.15}$$

With P solution of the algebraic Riccati equation:

$$P = A_d^T P A_d - \left(A_d P C^T + Q_{Nd}\right)^{-1}\left(C P A_d^T\right) + Q_d \tag{2.16}$$

2.7 Example of Kalman predictor application

In the following pages are presented the results obtained by the Kalman predictor for the run 8. The noise obtained from the constructed noise model through the Kalman predictor is compared to the real noise from experimental data.

The run 8 is characterized by the following parameters (considering the trajectory presented in Section 2.3):

- Height $= 8m$
- TAV $= 0.6 rad/s$, and therefore the circular path consists of three full circles
- Yaw Following active
- Average ambient light: 100 lux

The real trajectory followed by the drone is shown in Figure 2.27.

To start the Kalman predictor, all the vectors of predicted noises have the first component set to zero.

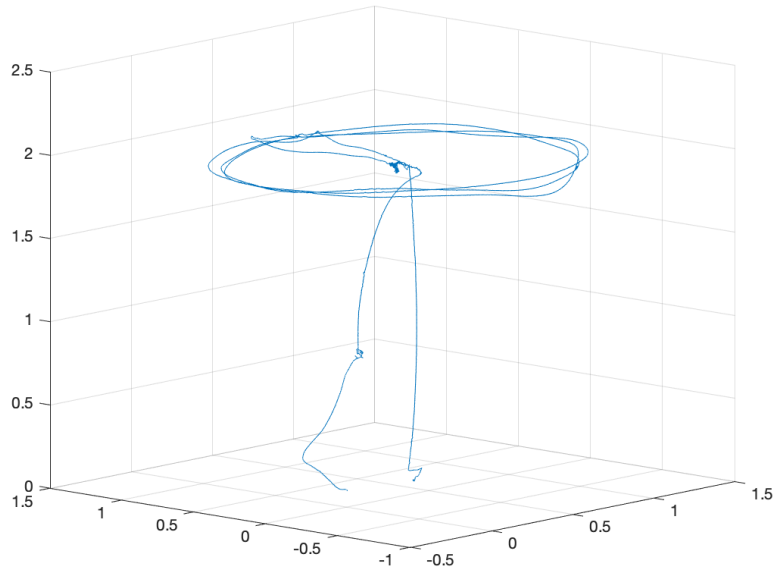

Figure 2.27: Trajectory followed by the drone in run 8.

2.7.1 East Axis

In the first plot of Figure 2.28, the values of position on the East axis for the run 8, obtained from the ZED camera and from the MOCAP, are shown. In the second plot their difference (the true total noise z_M) is represented, which is the set of values that is taken as input by the ADEV. One can clearly see how this error grows in time.

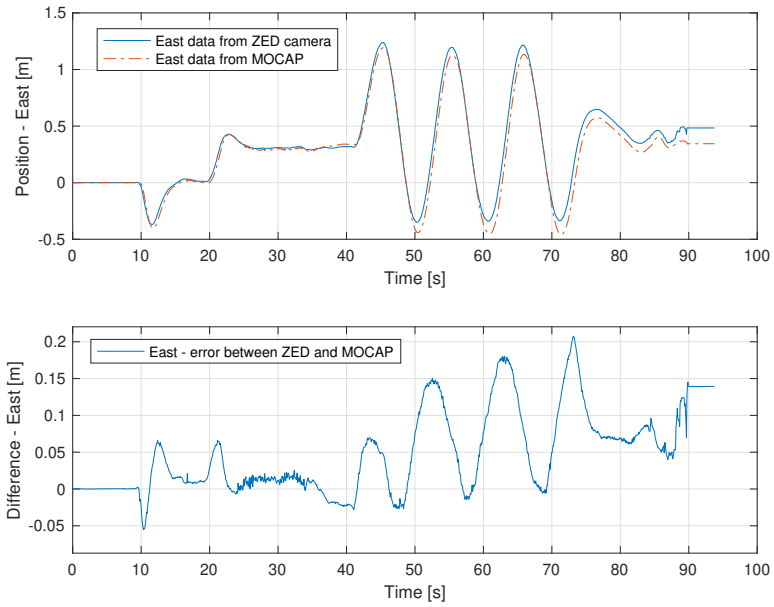

Figure 2.28: Position on East axis of run 8 from ZED camera and MOCAP, and their difference.

The noise coefficients of East axis for run 8 are (from the ADEV analysis): $N = 1e-4$, $K = 0.02$, $T_B = 0.1$, $Q_B = 1e-6$.

The simulation of the total noise z_d by the Kalman predictor, compared to the true noise z_M (error between ZED and MOCAP data) is shown in Figure 2.29, while their difference is shown in Figure 2.30. Looking at the difference, one can see that there are single points characterized by a huge difference between the predicted noise and the real one, but the average trend shows that the ADEV-based noise model, through the Kalman predictor, succeeds in following the real noise and quickly adapts to sudden oscillations. This happens also for axes North and Up, as shown in the next pages.

2.7.2 North Axis

In the first plot of Figure 2.31, the values of position on the North axis for the run 8, obtained from the ZED camera and from the MOCAP, are shown. In the

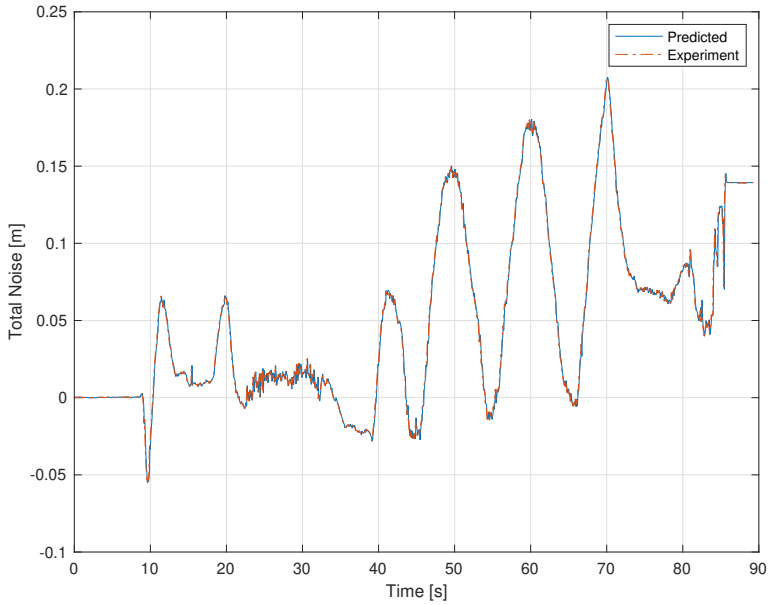

Figure 2.29: Results of the total noise z_d from the Kalman simulation, compared to the real noise z_M - East

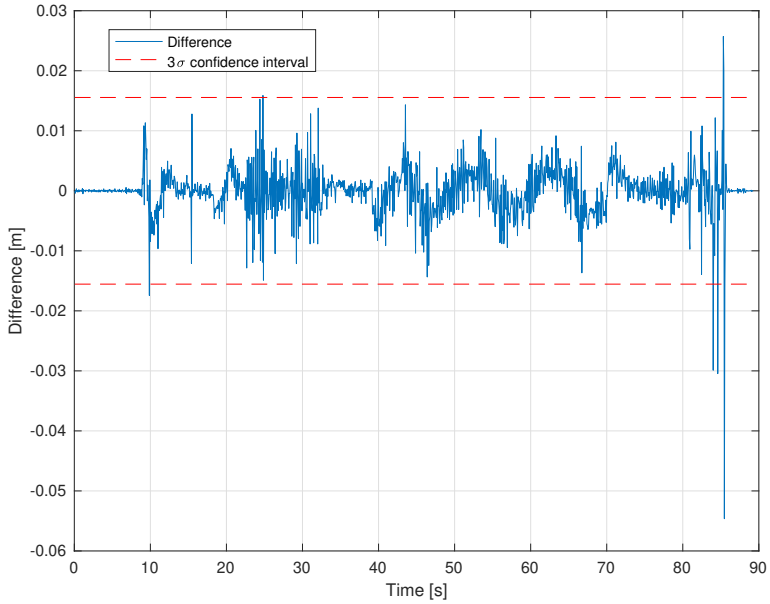

Figure 2.30: Difference between predicted noise z_d and true noise z_M - East

second plot is represented their difference.

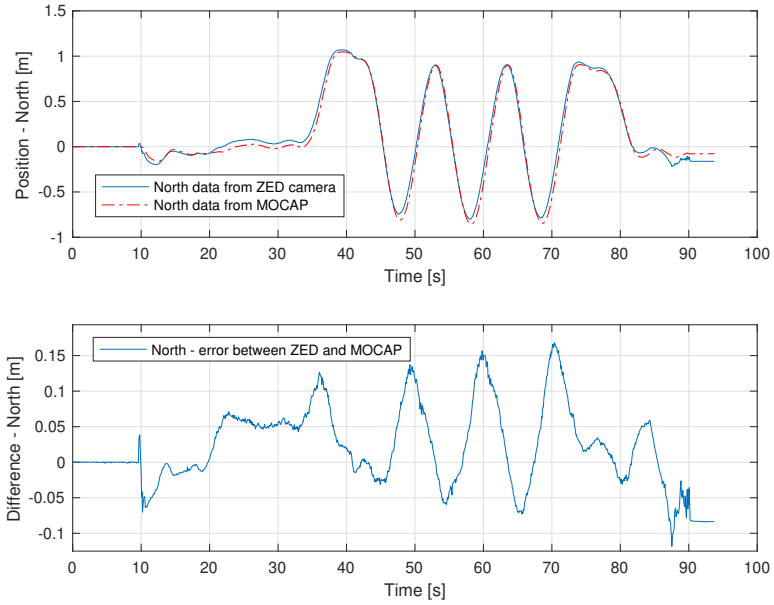

Figure 2.31: Position on North axis of run 8 from ZED camera and MOCAP, and their difference.

The noise coefficients of North axis for run 8 are: $N = 1.4e-4$, $K = 0.02$, $T_B = 0.1$, $Q_B = 1e-6$.

The simulation of the total noise z_d by the Kalman predictor, compared to the true noise z_M is shown in Figure 2.32, while their difference is shown in Figure 2.33.

2.7.3 Up Axis

In the first plot of Figure 2.34, the values of position on the Up axis for the run 8, obtained from the ZED camera and from the MOCAP, are shown. In the second plot is represented their difference.

The noise coefficients of Up axis for run 8 are: $N = 0$, $K = 0.03$, $T_B = 0.1$, $Q_B = 1e-7$.

The simulation of the total noise z_d by the Kalman predictor, compared to the true noise z_M is shown in Figure 2.35, while their difference is shown in Figure 2.36.

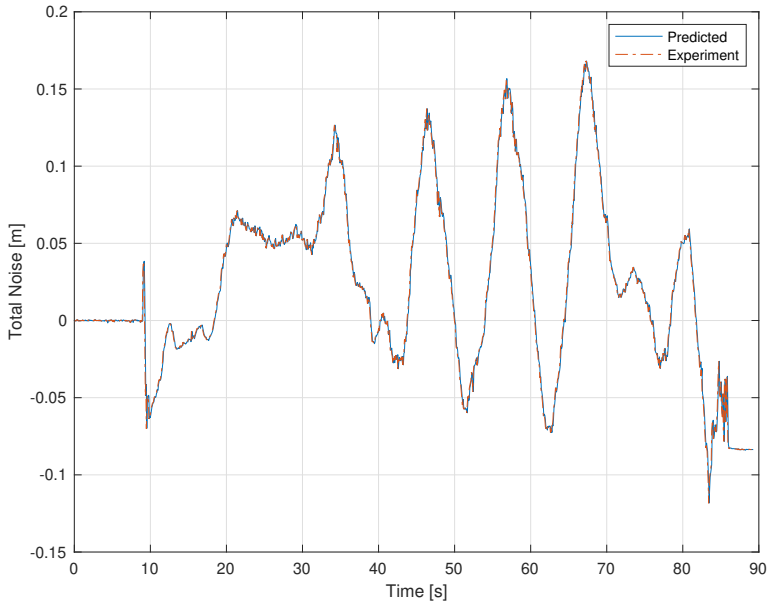

Figure 2.32: Results of the total noise z_d from the Kalman simulation, compared to the real noise z_M - North

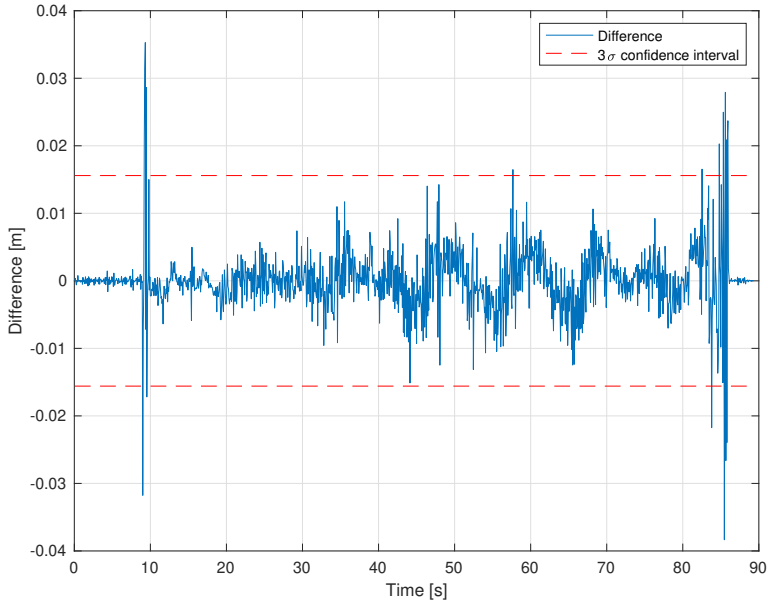

Figure 2.33: Difference between predicted noise z_d and true noise z_M - North

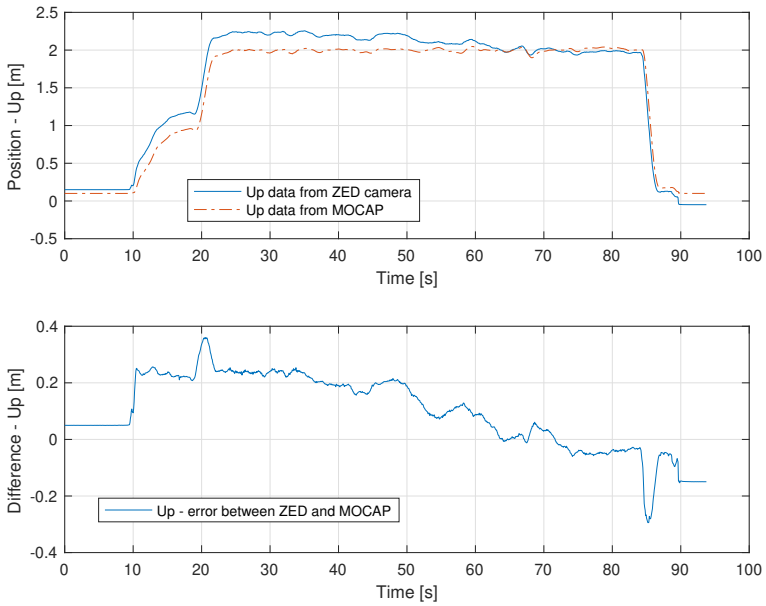

Figure 2.34: Position on Up axis of run 8 from ZED camera and MOCAP, and their difference.

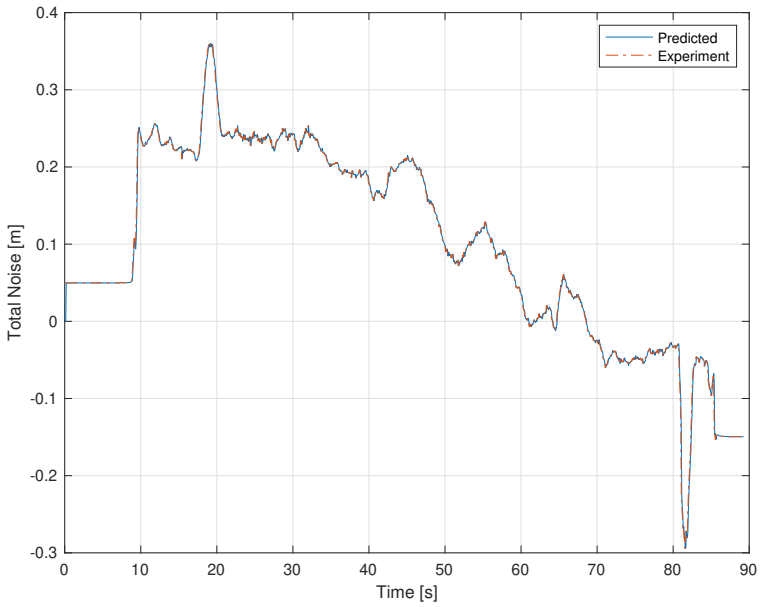

Figure 2.35: Results of the total noise z_d from the Kalman simulation, compared to the real noise z_M - Up

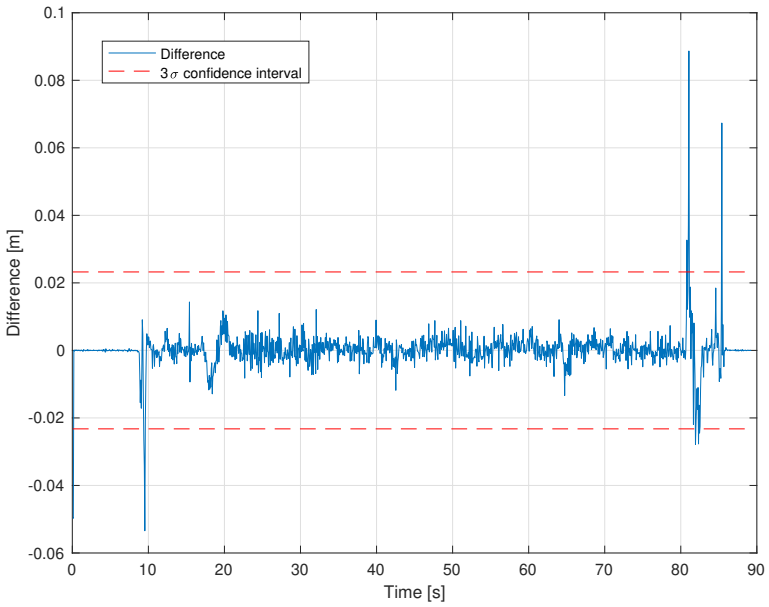

Figure 2.36: Difference between predicted noise z_d and true noise z_M - Up

Conclusions

The aim of this thesis was to characterize the dynamics of the noise affecting the measurements of position of a drone's visual odometry system.

The noise has been studied by means of a statistical, time-domain-based method called Allan variance, which is usually used in IMU analysis framework. In chapter one the AVAR has been presented, and the most common noises types have been introduced, along with their ADEV representations. Then, an example of how the noise coefficients can be obtained from the ADEV has been shown. The first chapter ends with the explanation of the procedure to write, given specific conditions on the nature of the noises involved, the continuous-time state space representation of the dynamics of the noise.

In the second chapter, the AVAR analysis of a drone's visual odometry system has been presented. In the first part, the experimental setup has been described. Sixteen different experiments have been performed, each one identified by a different choice of four different parameters: height of the trajectory, speed, yaw following and ambient light.

The results of the experiments have been presented and have been compared to each other. In several cases, patterns appeared about how different flight and environmental conditions can influence the noise coefficients.

The last part of the second chapter focuses on the time discretization of the state-space representation and on the construction of a Kalman predictor, to compare the AVAR-based noise model to the real noise measured during the experiments. An example of application of the predictor is then shown, with real data from one of the experiments.

In conclusion, are here reported some possible improvements of the discussed analysis and simulation methods:

- To better characterize the odometry error in terms of noise coefficients, noises without a direct state space representation may be used, and the final state space model may be obtained by the total estimated PSD of the noises through approximation techniques.

- A more exhaustive and comprehensive analysis on how the trajectory and the environmental conditions modify the noise coefficients can be performed.

More precise noise coefficients may improve also the behaviour of the predictor, especially for high frequency oscillations.

Bibliography

[1] Naser El-Sheimy, Haiying Hou, and Xiaoji Niu. Analysis and modeling of inertial sensors using allan variance. *IEEE Transactions on instrumentation and measurement*, 57(1):140–149, 2007.

[2] David W Allan. Statistics of atomic frequency standards. *Proceedings of the IEEE*, 54(2):221–230, 1966.

[3] Ieee standard definitions of physical quantities for fundamental frequency and time metrology—random instabilities. *IEEE Std Std 1139-2008*, pages c1–35, 2009.

[4] William J Riley. *Handbook of frequency stability analysis*. US Department of Commerce, National Institute of Standards and Technology . . . , 2008.

[5] David A Howe, DU Allan, and JA Barnes. Properties of signal sources and measurement methods. In *Thirty Fifth Annual Frequency Control Symposium*, pages 669–716. IEEE, 1981.

[6] Haiying Hou. *Modeling inertial sensors errors using Allan variance*. Citeseer, 2004.

[7] P. Lesage and T. Ayi. Characterization of frequency stability: Analysis of the modified allan variance and properties of its estimate. *IEEE Transactions on Instrumentation and Measurement*, 33(4):332–336, 1984.

[8] Niu et al. Using allan variance to analyze the error characteristics of gnss positioning. *GPS Solutions*, 18, 04 2014.

[9] D. Scaramuzza and F. Fraundorfer. Visual odometry [tutorial]. *IEEE Robotics Automation Magazine*, 18(4):80–92, 2011.

[10] Zed website: https://www.stereolabs.com/zed/.

[11] Optutrack website: https://optitrack.com.

[12] N. J. Kasdin. Discrete simulation of colored noise and stochastic processes and 1/f/sup /spl alpha// power law noise generation. *Proceedings of the IEEE*, 83(5):802–827, 1995.

[13] Jay A Farrell, Felipe O Silva, Farzana Rahman, and Jan Wendel. Imu error state modeling for state estimation and sensor calibration: A tutorial. 2019.